Coupling cellular drug-target engagement to downstream pharmacology with CeTEAM

Nicholas C.K. Valerie[1,*], Kumar Sanjiv[2], Oliver Mortusewicz[2], Si Min Zhang[2], Azita Rasti[2], Marie-France Langelier[3], Daniel Rehling[4], Adam Throup[2], Matthieu Desroses[2], Prasad Wakchaure[2], Ingrid Almlöf[2], Seher Alam[1], Johan Boström[1], Luka Bevc[2], Pål Stenmark[4], John M. Pascal[3], Thomas Helleday[2], Brent D.G. Page[2,5,†], and Mikael Altun[1,†]

[1]Science for Life Laboratory, Division of Clinical Physiology, Department of Laboratory Medicine, Karolinska Institutet, Karolinska University Hospital; Huddinge, SE-141 52, Sweden.

[2]Science for Life Laboratory, Department of Oncology-Pathology, Karolinska Institutet; Solna, SE-171 65, Sweden.

[3]Département de Biochimie and Médecine Moléculaire, Faculté de Médecine, Université de Montréal; Montréal, QC H3C 3J7, Canada.

[4]Department of Biochemistry and Biophysics, Stockholm University; Stockholm, SE-114 19, Sweden.

[5]Faculty of Pharmaceutical Sciences, University of British Columbia; Vancouver, V6T 1Z3, Canada.

*Corresponding author. Email: nicholas.valerie@ki.se

†These authors contributed equally

Abstract

Cellular target engagement technologies are reforming drug discovery by enabling quantification of intracellular drug binding; however, concomitant assessment of drug-associated phenotypes has proven challenging. We have developed cellular target engagement by accumulation of mutant (CeTEAM) as a platform that can seamlessly evaluate drug-target interactions and phenotypic responses in a single multiparametric experiment. In the presence of binding ligand, accumulation of an initially unstable target protein acts as a biosensor that permits holistic assessment of drug pharmacology under physiological conditions. We demonstrate this proof-of-concept by uncoupling target binding from divergent cellular activities of MTH1 inhibitors, repurposing the R139C variant to dissect complex NUDT15-thiopurine interactions, and profiling the live-cell dynamics of DNA trapping by PARP inhibitors. Further, PARP1-derived drug biosensors facilitated multimodal *ex vivo* analysis of drug-target engagement and non-invasive tracking of drug binding in live animals. CeTEAM empowers real-time, comprehensive characterization of target engagement by bridging drug binding events and their biological consequences.

Introduction

Establishing drug-target engagement in cells is a central pillar of drug discovery that is crucial for combating attrition during the development of new medicines[1-4]. Cellular target engagement techniques, such as CETSA[5], have enabled advanced understanding of biophysical protein-ligand interactions and how they can translate to biological or therapeutic effects. Despite their impact, current techniques provide incomplete characterizations of drug pharmacology because they are unable to seamlessly integrate downstream cellular responses. Commonly, this is because the cellular environment must be perturbed to detect the drug binding event, which can complicate the interpretation of relevant biology in the unperturbed state[6, 7]. Therefore, the development of novel, orthogonal approaches to understand drug pharmacology more holistically are warranted.

One avenue to circumvent this issue involves the direct modulation of protein abundance in a cellular setting, which is governed by the orchestrated interplay of protein translation and destruction (proteolysis). Binding of small molecules to a protein typically confers increased stability towards denaturation and proteolysis, thus disfavoring protein unfolding[8], but this would otherwise be difficult to observe in an unperturbed cellular environment. Protein turnover can also be increased by facilitating the "availability" to the cellular proteolysis machinery[9]. The quality control system actively patrols intracellular protein stability, thereby regulating general proteostasis, as well as the timely destruction of potentially detrimental misfolded proteins[10]. Conditional molecular biosensors[11] and destabilizing domains[12] can exploit these regulatory pathways by rapidly accumulating in response to ligand binding, which decreases turnover rate of the protein *via* the ubiquitin-proteasome and/or autophagy systems by stabilizing a partially folded destabilized intermediate[13]. These approaches have employed engineered, destabilized missense variants and degron tags, which act as accelerants for protein turnover, to shed light on metabolic dynamics[11] and protein function[14] under physiological settings.

Here, we show that known destabilizing missense mutants of notable preclinical and clinical drug targets can function as stability-dependent biosensors that enable comprehensive interrogation of drug-target interactions. Drug binding events are conveyed by increases in biosensor abundance that are readily combined with downstream pharmacological events in a single experimental interface. We demonstrate this proof-of-concept by first uncoupling target

binding from divergent cellular activities of different MTH1 inhibitors utilizing a V5-G48E missense mutant. Next, we repurpose the NUDT15 R139C variant, an established prognostic factor in thiopurine sensitivity, as an HA-tagged biosensor to dissect complex NUDT15-thiopurine interactions. Finally, we shift our attention to profiling the live-cell dynamics of PARP1 binding and DNA trapping by clinical/preclinical PARP inhibitors with a synthetic mutant of PARP1, L713F-GFP, which enables the triaging of prospective PARPi by trapping potential at scale. Fluorescent and bioluminescent PARP1-derived drug biosensors further facilitated multimodal *ex vivo* analysis of drug-target engagement and non-invasive detection of drug binding in live animals, respectively, thereby demonstrating the translatability of CeTEAM to *in vivo* applications. We envision that CeTEAM will be a powerful tool that enables real-time, holistic characterization of cellular drug-target engagement by linking drug binding to phenotypic events.

Results

Known destabilizing missense variants can function as drug biosensors

Structural destabilization of proteins is a common outcome of missense mutations observed across the proteome[15]. Based on this principle, there have been many successful examples of engineered biosensors that are conditionally stabilized by cognate binding ligands, thereby leading to their rapid accumulation in cellular environments[11-13]. We then asked if this phenomenon was more broadly applicable to naturally occurring missense variants or those synthetically generated for other purposes. When we introduced known destabilized variants of human NUDT15[16], MTH1[17], or PARP1[18] into cells, their low abundance was rescued by proteasome inhibitors, confirming their rapid turnover (**Extended Data Fig. 1**, **Supplementary Discussion**). Interestingly, this stabilization could be recapitulated by *bona fide* inhibitors in a time- and dose-dependent manner that was unrelated to their expression, while known inactive molecules did not (**Fig. 1a-c, Extended Data Fig. 1**). This implied that accumulation of the destabilized proteins was a result of direct binding to and stabilization by small molecule inhibitors, not a feedback expression regulatory circuit.

In the context of pharmacology, we then reasoned that this phenomenon could be generally adapted to monitor cellular target engagement and drug-related phenotypes in a single assay, which we call cellular target engagement by accumulation of mutant (CeTEAM; **Fig. 1d**), thereby directly linking drug binding events to resultant phenotypic changes. We then proceeded to explore insights afforded by this approach within the context of the target proteins.

Exploring divergent cellular activities of MTH1 inhibitors with an MTH1 drug biosensor

MTH1 (NUDT1) is a sanitizer of the oxidized nucleotide pool that initially garnered immense interest as an oncology drug target[19-21]. Subsequent investigations have highlighted potent and structurally diverse inhibitors (MTH1i) that engage MTH1 in cells but cannot reproduce the anti-cancer activity of earlier molecules (**Fig. 2a**)[22-24]. To reconcile these differences, we utilized an unstable MTH1 G48E variant reported as a possible familial nonpolyposis association factor[17]. Importantly, this mutant retains the ability to bind to MTH1i *in vitro* and demonstrates a comparable shift in thermal denaturation resistance as WT MTH1 following drug binding[17]. We found that all the reported inhibitors induced accumulation of a V5-MTH1 G48E drug biosensor in cells but had no discernable effect on a WT version of the transgene after 24 hours by pooled

western blot analysis (**Fig. 1a**, **Fig. 2b)**. We simultaneously probed for additional markers related to MTH1i cellular activities – specifically mitotic progression (histone H3 [HH3] Ser10) and DNA damage (γH2A.X)[25-27]. Inspection of these markers revealed that only TH588 induced DNA damage and mitotic arrest despite similar stabilization of V5-G48E by all tested molecules (**Fig. 2b**).

To clarify this observation at the single cell level, flow cytometry experiments were performed with clonal V5-G48E cells to simultaneously track V5 and HH3 Ser10 signals, as well as DNA content by Hoechst 33342 staining, after treatment with 2.5 μM TH588 or 1 μM AZ19 (**Fig. 2c**). Single cell clones of V5-G48E cells were utilized to maximize robustness and uniformity when correlating to downstream MTH1i events. This analysis revealed that AZ19 stabilized the MTH1i biosensor better than TH588, although both compounds significantly increased V5 signal throughout the cell population compared to a DMSO control (**Fig. 2d**). Notably, however, cells treated with TH588 had an overall increased proportion of HH3 Ser10 positivity that coincided with DNA content perturbations – namely an increase in the G1/G0 and dead cell (sub-G1) populations (**Fig. 2e-g**).

We then sought to understand the interrelatedness of MTH1i target binding to the observed mitotic arrest seen in TH588-treated cells. To this end, HH3 Ser10 and Hoechst intensities were visualized in the context of V5 high signal, classified as greater or equal to the top 2% of the DMSO control intensity (**Fig. 2h**). While V5 enriched cells in the DMSO control clustered in corresponding G2/M populations, in line with the notion of higher per-cell protein content prior to cell division, MTH1i-treated cells were ubiquitously spread throughout the cell cycle (**Fig. 2i**). However, TH588-stabilized V5-G48E cells had a four-fold enrichment in the mitotic population compared to AZ19-treated counterparts (**Fig. 2j**), which is in line with previous observations investigating this difference in activity[26, 27]. Collectively, our studies confirm that TH588 triggers the mitotic surveillance pathway[25] and that this is likely independent of MTH1 binding. Thus, CeTEAM can differentiate target engagement from divergent biological activities among structurally dissimilar molecules.

Illuminating complex NUDT15-thiopurine interactions with the R139C common missense variant

NUDT15 deactivates the nucleoside analog antimetabolite, thiopurine, by hydrolyzing the active triphosphates and limiting DNA damage-induced toxicity[16, 28]. Several destabilizing variants of NUDT15 have been associated with clinical thiopurine intolerance[28] and can be stabilized towards thermal denaturation by NUDT15 inhibitors (NUDT15i) *in vitro*[29], including R139C, which is known to be rapidly degraded by the proteasome[16]. When cells expressing an HA-tagged R139C variant were incubated with thioguanine, we saw increased incorporation-related DNA damage but, interestingly, also an accumulation of HA-R139C (**Fig. 3a**). Intrigued by the possibility that thioguanine or its metabolites could act as inhibitors, we then screened a small set of thiopurine metabolites and confirmed that NUDT15 activity can be inhibited by these species – most notably 6-thio-GDP (**Fig. 3b**).

This prompted us to investigate other previously available (NSC56456)[30] or in-house developed (TH8228 and TH8234) thiopurine analogs as potential NUDT15i (**Fig. 3c**). An enzyme-coupled malachite green inhibition assay determined that NSC56456 and TH8234 similarly inhibited dGTP hydrolysis (IC_{50} = 355 and 375 nM, respectively), albeit less potently than optimized NUDT15i[29-31], while TH8228 was completely inactive (**Fig. 3d**). For further insight, a NUDT15-NSC56456 co-crystal structure was solved at 1.8 Å resolution and illustrates that the NSC56456 binding modality is highly similar to 6-thio-GMP[16] in the enzyme active site (**Extended Data Fig. 2**). These data also imply that the methylthio moiety present in TH8228 should discourage NUDT15 binding due to steric clashing within the hydrophobic pocket, which is reflected in the inhibition assay (**Fig. 3d**). In line with this observation, NSC56456 stabilized wild-type NUDT15 by DSF assay, whereas TH8228 did not (**Fig. 3e**). As before[16], NUDT15 R139C had a significantly lower melting temperature than wild-type (T_m; 47 versus 56 ºC, respectively) but was comparably stabilized by NSC56456 (ΔT_m = 7 and ΔT_m = 6ºC, respectively). In tandem with initial observations (**Fig. 1b** and **Fig. 3a**), these data suggest that NUDT15 R139C can effectively accommodate and be stabilized by binding ligands *in vitro* and in the intracellular environment.

Triaging of *bona fide* inhibitors can be complicated by equating on-target binding/inhibition to intended phenotypic responses and *vice versa*. We then sought to understand the behavior of our thiopurine analogs and how they affect NUDT15-mediated thioguanine (6TG)

toxicity in cells using a CeTEAM approach. Previous work by us and others has demonstrated that genetic or pharmacological ablation of NUDT15 activity decreases thiopurine toxicity thresholds by approximately one order of magnitude[16, 28, 31]. We therefore established a high-content immunofluorescence microscopy CeTEAM workflow that profiled these compounds alone and in combination with low-dose 6TG using HA-tagged NUDT15 R139C as a NUDT15i reporter (**Fig. 3f**). First, we confirmed that 200 nM 6TG alone neither increased HA-R139C and γH2A.X signals nor affected the cell cycle (**Extended Data Fig. 3a-c**). By initial observation, NSC56456 both dose-dependently stabilized NUDT15 R139C and enhanced thioguanine-mediated DNA damage, therefore upholding its status as a *bona fide* NUDT15i, and was easily distinguished from molecules that either mimicked thiopurine prodrugs (TH8234) or were unable to bind NUDT15 (TH8228; **Fig. 3g, Extended Data Fig. 3d-f, Supplementary Fig. 1**).

To determine the link between NUDT15 binding and potentiation of 6TG-mediated toxicity, multiparametric CeTEAM analyses were performed at the single cell and global level. Single cell mapping revealed that HA-R139C stabilization occurs independently of cell cycle, although as would be expected, a majority of γH2A.X-positive cells were stalled in S/G2 phases following co-treatment with 6TG (**Fig. 3h**). On a macro scale, we reasoned that triaging of potential NUDT15i based on HA-R139C stabilization and markers of 6TG potentiation can theoretically be categorized under four groups: non-responder, stabilizer, potentiator, or non-specific (**Fig. 3i**) – where potentiation of 6TG toxicity can be thought of as an expected outcome and non-specific DNA damage would be considered an unexpected outcome. In this context, stabilizers *can* transition to potentiators upon addition of 6TG but may not always do so (*e.g.*, if utilizing a ligand that purely affects target protein stability without inhibiting enzymatic activity). Applying this logic, NSC56456 is clearly a stabilizer that also potentiates 6TG, whereas TH8228 is a non-responder (**Fig. 3j**). Uniquely, TH8234 is a potentiator irrespective of 6TG addition, which strongly suggests it is a thiopurine pro-drug. Collectively, the results emphasize that thiopurine mimetics are putative chemical starting points for developing new NUDT15 probes[30]. More importantly, CeTEAM-based exploration of thiopurines highlights their complex relationship toward cellular NUDT15 and enabled the identification of NSC56456 as a genuine NUDT15i from a pool of similar, biochemically equipotent molecules.

Validation of PARP1 L713F as a PARPi biosensor

To further showcase the power of our approach, a biosensor system was developed for PARP1, an established drug target for multiple clinical indications. PARP1 L713F is a synthetic gain-of-function mutant that increases flexibility between the HD and ART domains, conferring both instability and DNA-independent PARylation activity[18, 32]. Purified PARP1 WT and L713F catalytic domains were comparably stabilized by clinical-grade PARP inhibitors (PARPi) – with L713F having a decreased baseline thermal stability (41.9 versus 47.4 ºC; **Extended Data Fig. 4a-c**) – thereby supporting its amenability to CeTEAM analysis (**Fig. 1c**).

PARP1 is recruited to sites of DNA damage and orchestrates the DNA damage response (DDR) *via* catalysis of polyADP-ribose (PAR)[33]. We then asked if PARP1 L713F could bridge the biophysical detection of PARPi target engagement to relevant PARP1 biology. As previously reported[34], we saw that PARP1 L713F-GFP is still recruited to damaged DNA in response to laser microirradiation, albeit with slightly attenuated kinetics (**Extended Data Fig. 4d and e**). Fluorescence recovery after photobleaching (FRAP) experiments also confirmed that PARP1 L713F is less mobile than WT PARP1, presumably due to greater retention on DNA resulting from increased flexibility of the L713F HD domain (**Supplementary Fig. 2**)[35]. We then wanted to understand how downstream DDR markers (PAR and γH2A.X) were affected following microirradiation in PARP1 WT or L713F cells pre-treated with PARPi for 1 or 24 hours (**Extended Fig. 4f**). L713F-GFP biosensor levels were significantly elevated after only one hour of PARPi (**Extended Data Fig. 4g, Extended Data Fig. 5a and b**). In both untreated WT and L713F PARP1 cells, PAR signal elevated initially then returned to baseline following DNA damage, while γH2A.X temporally increased (**Extended Data Fig. 5c and d**). Basal PAR and γH2A.X were elevated in L713F cells compared to WT, as described previously, but obvious signs of toxicity were not observed (**Extended Data Fig. 5c and d**, **Supplementary Fig. 3**, **Supplementary Discussion**). Simultaneous analysis of GFP and PAR intensity in single cells revealed that drug-induced stabilization of L713F-GFP highly correlated with PAR suppression as a proximal marker of PARPi target engagement but, like WT PARP1, did not affect corresponding γH2A.X formation after DNA damage (**Extended Data Fig. 4g**). These results suggest that PARP1 L713F-GFP faithfully reflects PARPi binding in a cellular context.

Dynamic profiling of PARPi binding and DNA trapping in live cells at scale

An underlying factor dictating clinical responses to some PARPi is the inherent ability to "trap" PARP onto DNA and induce replication stress in cancer cells, which is independent of PARPi inhibitory activity[36-38]. However, the associated toxicity of trapping may be undesirable for other indications, such as neurodegenerative diseases, where enzymatic inhibition would suffice[39]. Known trapping PARPi caused significant PARP1 trapping and replication stress at later time points (**Fig. 4a and b, Extended Data Fig. 5e-h, Supplementary Fig. 2**), reflecting the increased retention of PARP1 on DNA elicited by some inhibitors[38]. Nonetheless, detailed characterization of trapping dynamics in relation to PARP1 binding has not been elucidated previously.

To survey trapping dynamics in a larger cohort of PARPi, we then employed CeTEAM with multiplexed live-cell fluorescent microscopy to concurrently track dose-dependent L713F-GFP accumulation and S/G2-phase shifts in DNA content as a surrogate for replication stress (**Fig. 4c, Supplementary Fig. 4**)[40]. All the clinical PARPi effectively stabilized L713F-GFP but exhibited differential trapping ability that mirrored reported inhibitory and trapping rankings (**Fig. 4d and e, and Supplementary Fig. 5**)[41]. Dose-dependent stabilization of L713F-GFP followed a sigmoidal saturation profile that permitted ranking of PARPi based on their observed stabilization EC_{50}s. Of note, talazoparib was most potent by both criteria and followed by olaparib/niraparib, whereas iniparib, a now debunked PARPi, failed to induce biosensor accumulation in any capacity[5, 42]. While veliparib was equipotent to other clinical inhibitors for PARP1 binding, it was vastly inferior at trapping, as effects only materialized in the micromolar range. Remarkably, the PARP1-GFP biosensor could detect binding of the relatively impotent 3-aminobenzamide (3-AB) in the near-millimolar range. 3-AB treatment also induced a G1-phase delay, as previously reported[43]. A two-dimensional dose-resolved analysis revealed that trapping phenotypes were apparent only after detectable PARP1 binding in all cases, although the extent of discrepancy between target engagement and trapping EC_{50}s varied among inhibitors tested (**Fig. 4f**). Accordingly, single cell evaluation underscored that cell populations treated with trapping PARPi are clearly distinguished from unperturbed control cells (**Fig. 4g**). This trapping trend was also observed by staining fixed cells for other DDR markers of replication stress, p-CHK1 Ser345 (**Extended Data Fig. 6, Supplementary Fig. 6**) or γH2A.X (**Extended Data Fig. 6, Supplementary Fig. 7**). Thus, PARP1 L713F-GFP is an effective rheostat for live-cell profiling

of the potential DNA retention associated with PARPi binding and is, therefore, useful for triaging inhibitors based on their trapping potential.

Multimodal assessment of in vivo PARPi target engagement ex vivo

We then sought to assess CeTEAM in animal models, as favorable *in vivo* pharmacokinetic/pharmacodynamic (PK/PD) profiles are crucial milestones in preclinical drug discovery that are reflective of target engagement and functional effects in desired tissues[4]. To evaluate the PARPi biosensor *in vivo*, we first paired L713F-GFP with a complementary mCherry reporter that effectively normalized quantification of PARPi target engagement (**Fig. 5a-c, Supplementary Fig. 8**). This not only enabled straightforward identification of target cells by microscopy (**Fig. 5b**, **Supplementary Fig. 8c and d**) or flow cytometry (**Fig. 5c**, **Supplementary Fig. 8e**) but also the ability to quantify the fraction of target cells demonstrating PARPi binding to PARP1, which is particularly well-suited for heterogeneous *in vivo* environments.

Mice harboring subcutaneous L713F-GFP/mCherry tumors were then systemically administered niraparib, which has excellent oral bioavailability[44], for two consecutive days prior to tumor excision and evaluation of target engagement (**Fig. 5d**). Niraparib treatment dose-dependently stabilized L713F-GFP when measured by either live-cell flow cytometry (**Fig. 5e and f**, **Extended Data Fig. 7a and b**) or western blot (**Fig. 5g and h**, **Extended Data Fig. 7c**) following normalization to mCherry signal. Staining of tumor cross-sections also revealed a high degree of heterogeneity in niraparib penetrance with systemic administration, thereby revealing the challenge of nonuniform drug exposure in tumors and tissues (**Fig. 5i**, **Extended Data Fig. 7d and e**). Niraparib distribution within the tumors was generally poor (**Fig. 5j**, **Extended Data Fig. 7f**) – where dose-dependent differences became more obvious when restricting the analysis to higher L713F-GFP signal intensities (**Fig. 5k**), which may be at least partially attributed to the poor vascularization often seen in HCT116 xenografts[45, 46]. Furthermore, these data underscore that standard measures of drug distribution (*e.g.*, plasma levels) paint an incomplete picture of target occupancy. Thus, *ex vivo* CeTEAM analyses can provide unique spatio-temporal and multimodal insight to drug-target interactions *in vivo*, such as how tumor heterogeneity affects drug exposure and responsiveness.

Non-invasive detection of PARPi engagement in live animals enabled by a dual luciferase biosensor system

An enticing implication of the CeTEAM approach is the possibility to track drug-target engagement in living systems in a non-invasive manner. As a prerequisite to test the capacity of CeTEAM in live animals, we found that PARP1 L713F is also amenable to nanoluciferase (nLuc) fusions (**Extended Data Fig. 8a and b)**, which enabled robust and sensitive detection of PARPi binding with lysed (**Extended Data Fig. 8c-e**) or intact cells (**Extended Data Fig. 8f-j**). We then complemented the nLuc biosensor with an akaLuc reference, a red-shifted variant of firefly luciferase[47], to normalize PARP1 binding signals (**Fig. 6a**, **Extended Data Fig. 9a and b**). akaLuc activity was lost following detergent-mediated lysis (**Extended Data Fig. 9c and d**), so both luminescence readings were performed with live cells using a spiral averaging feature to account for uneven distribution of cells in the wells. Despite clear spectral separation between nLuc and akaLuc (**Extended Data Fig. 9e)**, we determined that sequential detection enabled optimal normalization of PARP1 target engagement and eliminated any signal interference (**Extended Data Fig. 9f-m**).

Harnessing the high sensitivity of bioluminescence, PARP1 L713F-nLuc stabilization was detectable in as little as one hour after veliparib addition, while the dynamic range of the assay was maximal around 24 hours (**Fig. 6b**). Intriguingly, the apparent potency of treatment, expressed as EC_{50} values, did not vary with either time (**Fig. 6b**) or biosensor abundance (**Fig. 6c; Supplementary Fig. 9**), suggesting that this system is a robust methodology for rapidly evaluating cellular target engagement. One appealing prospect of a luminescence-based CeTEAM detection platform is the possibility to seamlessly scale assays for high-throughput analyses. In this vein, the PARP1 L713F-nLuc biosensor consistently scored signal-to-background (S/B) ratios above 6 and Z' values, a measure of the quality of a potential screening assay, greater than 0.5 in all tested cell lines and expression systems – indicating that luminescence-based CeTEAM iterations can reliably be extended to high-throughput screening campaigns for novel small molecule binders (**Extended Data Fig. 8k**)[48].

The bioluminescent readout further enabled quantitative detection of niraparib target engagement in live animals using fluorofurimazine, an *in* vivo-optimized nLuc substrate[49], when normalized to akaLuc signal (**Fig. 6d-f, and Extended Data Fig. 10**). As with the GFP variant,

two systemic doses of PARPi were sufficient for clear detection of PARP1 L713F-nLuc binding in subcutaneous HCT116 tumors (**Fig. 6d-f**) and was remarkably consistent across multiple experiments (**Extended Data Fig. 10c and d**). We were also able to confirm this finding following tumor excision and luminescence detection *ex vivo*, and, as seen with *in vitro* experiments, akaLuc luminescence effectively normalized PARP1 L713F-nLuc signals on a per-tumor basis (**Fig. 6g**). *Ex vivo* validation experiments also clearly demonstrated a greater fold-change of PARP1 L713F-nLuc signal in niraparib-treated tumors over controls, presumably due to tissue absorption of blue-shifted nLuc emissions (**Fig. 6h**)[50]. Despite this drawback, reliable measures of PARPi target engagement *in situ* are still possible in suboptimal settings with the brightness of an nLuc system. Taken together, the *in vivo* luminescence data with the PARP biosensor suggest that CeTEAM is a practical, yet powerful, approach to monitor drug binding in living animals, which has exciting applications for longitudinal studies modeling drug resistance mechanisms, among many others.

Discussion

Confirmation of target binding alone does not provide a complete pharmacological picture of a given test molecule. This is an important aspect of pre-clinical drug discovery that is often overlooked in early phases, despite representing a key branch point dictating future medicinal chemistry efforts. A somewhat surprising revelation from the literature is that cellular target engagement assays are primarily used as confirmatory assays and not as a tool to discover the "best" targeted molecules, in terms of on-target binding[6]. We envision that CeTEAM has the potential to shift this paradigm to earlier phases of drug discovery and development by enabling the rapid triaging of test molecules based on combined insights from biophysical and phenotypic components.

The downstream phenotypic events resultant from drug binding are difficult to protract in a single assay due to the perturbations inherent to current cellular target engagement assays. As an example, CETSA has effectively delivered cellular target engagement capabilities to the masses and its extension to global proteomics analysis offers exciting possibilities for deciphering drug mechanism(s)-of-action[5, 51]. However, the application of heat to detect binding events introduces confounding factors for interpreting the relationship between drug binding at elevated temperatures and downstream biology occurring at 37ºC (*i.e.*, multiple changing equilibria), which require in-depth deconvolution to accurately decipher[7]. Similarly, approaches such as DARTS[52] or HIPStA[53] require global modifications that are disruptive to cellular biological processes. Therefore, there is high value in novel assays that can more easily bridge this knowledge gap.

One of the key advantages we envisioned when conceptualizing CeTEAM is that target binding is evaluated under physiological conditions, implying that downstream pharmacological events can be directly related to observed binding events in cells. We applied this theory utilizing destabilizing missense mutants previously described for MTH1, NUDT15, and PARP1 to profile their cognate inhibitors in a relevant biological context and found high congruence with earlier findings. Following the initial observation that these mutants accumulated in cellular environments only following proteolytic inhibition or exposure to cognate ligands, we confirmed that the purified proteins were stabilized by ligand binding similarly to wild-type counterparts. This led us to the rationale that the proteolytic turnover of the destabilized variants is slowed by the stabilizing effect of ligand binding – presumably by masking degrons that would otherwise be exposed by missense

mutations at non-permissible temperatures[13] – and enabled the study of phenotypic changes in a setting with minimal disruption.

When target biology is well established, CeTEAM repeatedly demonstrated the ability to discern effects related to target binding from those that are not; however, it may not be possible to pinpoint specific off-target binding events. Nevertheless, the assay can be complemented with any number of phenotypic markers to guide experimenters towards an understanding of a given molecule's pharmacology. These could be skewed towards specific pathways related to the chosen target or cherrypicked from multiple pathways for unbiased profiling of downstream phenotypes. Such an approach would be advantageous in many instances where triaging of small molecules must be done at scale (*e.g.*, to understand phenotypic tendencies within inhibitor libraries, to determine novel biology related to a given target protein, *etc.*). Trends identified from CeTEAM can then be fine-tuned with orthogonal approaches, such as thermal proteome profiling[51], to rapidly identify desirable compounds and more completely understand their mechanism-of-action.

There are some important considerations when implementing CeTEAM into small molecule discovery campaigns. First, our approach requires the identification of suitable destabilizing protein variants. While many are identified serendipitously *via* disease linkages[15] or by randomized mutagenesis[12], modern computational and protein engineering technologies can be utilized for the directed evolution of future drug biosensors[11, 54, 55]. The destabilizing effect of a given missense mutation lies on a spectrum where locally destabilizing variants with minimal gross structural alterations would be preferred candidates for a CeTEAM approach[13, 15, 56]. For instance, each of the examples presented here was chosen at random but all share potential disruption of interhelical stability as an outcome of their respective point mutations. Another important aspect is the potential for functional perturbations by mutagenesis or overexpression, which may have implications for downstream biology. This should be investigated prior to screening with CeTEAM, although situations where applicable destabilizing mutants endogenously occur in primary or established cell lines or are engineered by genome editing could limit artifactual concerns. Additionally, due to the nature of the assay, it is possible for test molecules that interfere with proteolysis or selectively bind to the destabilized target to arise as false positives. Although inclusion of reference signals should mitigate this potential issue, like with all assays, counter-screening validation with analogous methods is beneficial.

In summary, the current work has demonstrated the potential utility of stability-dependent biosensors for drug discovery efforts from screening to *in vivo* quantification of target engagement. CeTEAM enables the direct association of cellular target binding with proximal or distal efficacy markers at cellular or subcellular resolution and high throughput. While biophysical assessment of target engagement is possible within one hour, the study can be protracted to follow downstream effects of test molecules. Of the many possible applications for this technology, perhaps the most valuable relate to high-throughput target engagement screening, identifying best-in-class pharmaceuticals, differentiating on- and off-target phenotypes of test molecules, deconvoluting protein functions, studying tumor heterogeneity and resistance mechanisms, as well as developing multiplexed *in vivo* PK/PD models. CeTEAM is, thus, a pragmatic, complementary approach for accelerating preclinical drug discovery and lead optimization efforts that combines desirable aspects of targeted and phenotypic assays in a highly translatable system.

Online Methods

Cell lines and culturing conditions

U-2 OS osteosarcoma and HEK293T embryonic kidney epithelial cells were obtained from the American Type Culture Collection (ATCC, Manassass, VA, USA). HCT116 and HCT116 3-6 colon carcinoma cells were originally obtained from Dr. Bert Vogelstein (Johns Hopkins University). U-2 OS and HEK293T cells were cultured in DMEM high glucose, GlutaMAX medium (Thermo Fisher Scientific), while HCT116 and HCT116 3-6 cells were cultured in McCoy's 5a, GlutaMAX medium (Thermo Fisher Scientific). For *in vitro* luciferase read-outs, FluoroBrite DMEM (Thermo Fisher Scientific) supplemented with GlutaMAX was used. All media were supplemented with 10% heat-inactivated fetal bovine serum (FBS) and penicillin/streptomycin. Cell cultures were maintained at 37 °C with 5% CO_2 in a humidified incubator. The cells were routinely screened for mycoplasma using the MycoAlert kit (Lonza Bioscience) and none were listed on ICLAC or known to be cross-contaminated.

Antibodies and chemicals

anti-HA probe (mouse monoclonal, sc7392), anti-GFP (rabbit polyclonal, sc8334), anti-GFP (mouse monoclonal, sc9996), anti-PARP1 (mouse monoclonal, sc8007), and anti -SOD1 (mouse monoclonal, sc17767) were obtained from Santa Cruz Biotechnology. anti-CHK1 (mouse monoclonal, 2360S), anti-p-CHK1 Ser345 (rabbit polyclonal, 2341S), anti-p-CHK1 Ser345 (rabbit monoclonal, 2348S), anti-p-Histone H2A.X Ser139 (γH2A.X, rabbit polyclonal, 2577S) were obtained from Cell Signaling. anti-NUDT15 (rabbit polyclonal, GTX32751) was purchased from GeneTex. anti-V5 tag (mouse monoclonal, 46-0705) was purchased from Invitrogen (now Thermo Fisher Scientific). anti-NUDT5 (rabbit polyclonal) was generated in-house as previously described[57]. anti-MTH1 (NUDT1, rabbit polyclonal, NB100-109) was obtained from Novus Biologicals. anti-p-Histone H3 Ser10 (rabbit polyclonal, ab5176) and anti-β-actin (mouse monoclonal, ab6276) were purchased from Abcam. anti-p-Histone H2A.X Ser139 (γH2A.X, mouse monoclonal, 05-636) and pan-ADP-ribose binding reagent (rabbit Fc tag, MABE1016) were obtained from Millipore. Donkey anti-mouse IgG IRDye 680RD (cat. no. 925-68072) and goat anti-rabbit IgG IRDye 800CW (cat. no. 925-32211) were purchased from Li-Cor. anti-mCherry (rabbit polyclonal, cat. no. PA5-34974), donkey anti-mouse IgG Alexa Fluor 488 (cat. no. A-21202), donkey anti-mouse IgG Alexa Fluor 555 (cat. no. A-31570), donkey anti-rabbit IgG

Alexa Fluor 568 (cat. no. A-10042), donkey anti-rabbit IgG Alexa Fluor 647 (cat. no. A-31573), goat anti-rabbit IgG Alexa Fluor 488 (cat. no. A-11008), and donkey anti-mouse IgG Alexa Fluor 647 (cat. no. A-31571) were purchased from Thermo Fisher Scientific.

Doxycycline hydrochloride (Sigma-Aldrich) was dissolved in MilliQ water (2 mg/mL) and used at 1 µg/mL. MG-132 (Z-Leu-Leu-Leu-al, Sigma-Aldrich) was dissolved in DMSO (10 mM stock) and used at 5 µM. 6-methylthio-GDP, 6-methylthio-GMP, 6-thio-GMP, and 6-thio-GDP were purchased from Jena Bioscience and dissolved in MilliQ water to 10 mM. NSC56456 was obtained from the NCI Developmental Therapeutics Program and later re-synthesized[30], while TH8228 and TH8234 were synthesized in-house (see Chemical synthesis and characterization section) but all were dissolved in DMSO. TH588, AZ19, IACS-4759 and BAY-707 were obtained or synthesized in-house as described previously[20, 22-24, 58]. Talazoparib, niraparib, olaparib, veliparib, and iniparib (SelleckChem) were dissolved in DMSO. 3-aminobenzamide (3-AB; Sigma-Aldrich) was dissolved in DMSO to a stock of 100 mM. All other inhibitors were dissolved at 10 mM. Furimazine was purchased as part of the Nano-Glo Assay kit (Promega), fluorofurimazine was obtained from Promega as a ready-to-use poloxamer-407 (P-407) desiccate that was reconstituted in sterile PBS[49], and akaLumine HCl (TokeOni; Sigma Aldrich) was dissolved in MQ water to 40 mM, aliquoted, and stored at -80ºC.

Chemical synthesis and characterization

Synthesis of TH008228 (9-cyclohexyl-6-(methylthio)-9H-purin-2-amine)

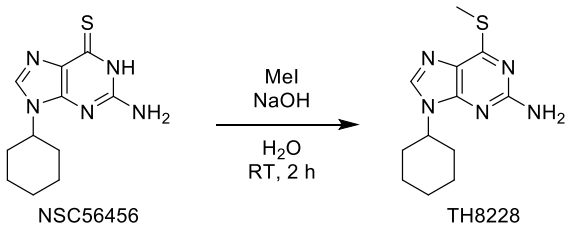

2-amino-9-cyclohexyl-1H-purine-6-thione (NSC56456, 10 mg, 0.040 mmol) was dissolved in 0.5 M NaOH (1 mL) and stirred for 10 min., after which time MeI (2 µL, 0.040 mmol) was added and stirred for 2 hours at RT. The product was purified by preparative HPLC to give 9-cyclohexyl-6-(methylthio)-9H-purin-2-amine (4.00 mg, 37.9% yield) as a white powder. ^{1}H NMR (400 MHz, DMSO-d_6) δ ppm 8.12 (s, 1H), 4.25 – 4.16 (obscured by water peak, m, 1H), 2.57 (s, 3H), 1.96 (d, J = 9.0 Hz, 2H), 1.80 (dt, J = 12.2, 7.3 Hz, 4H), 1.69 (d, J = 12.4 Hz, 1H), 1.47 – 1.31 (m, 2H), 1.29 – 1.20 (m, 1H). LCMS: *m/z* 254.2 $[M+H]^+$, Rt = 1.451 min., purity at 254 nm >95%

Synthesis of TH008234 (2-amino-9-(2-phenylpropan-2-yl)-1H-purine-6-thione)

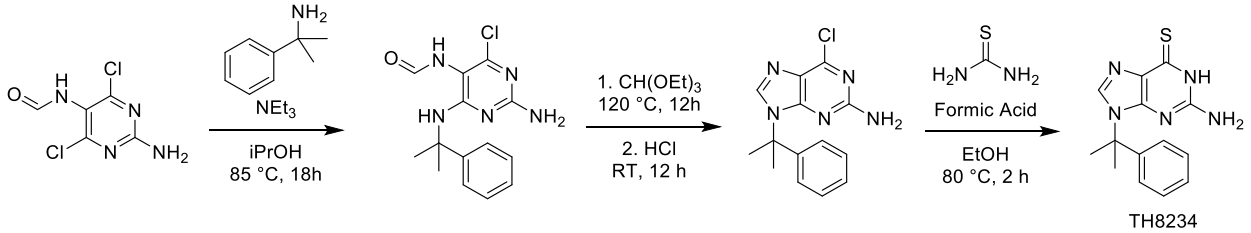

Step 1: N-{2-amino-4-chloro-6-[(2-phenylpropan-2-yl)amino]pyrimidin-5-yl}formamide

α,α-dimethylbenzylamine (29.4 mg, 0.217 mmol) was added to a stirred solution of N-(2-amino-4,6-dichloropyrimidin-5-yl)formamide (30 mg, 0.145 mmol) and NEt_3 (2 eq) in $^{i}PrOH$ (3 mL) and heated at 85 °C for 18 h. The reaction was cooled to RT, and the crude amino pyrimidine (44 mg, 99.3% yield) was collected by filtration.

Step 2: 6-chloro-9-(2-phenylpropan-2-yl)-9H-purin-2-amine

The crude amino pyrimidine (47 mg, 0.154 mmol) was dissolved in triethyl orthoformate (1.5 mL), heated at 120ºC for 12 hrs, then cooled to RT. HCl (0.05 mL, 12 M) was added and the reaction mixture was stirred for 12 hrs before concentrating under reduced pressure to give the crude 6-chloropurine (44 mg, 99.5% yield).

Step 3: 2-amino-9-(2-phenylpropan-2-yl)-3H-purine-6(9H)-thione

The crude 6-chloropurine (44 mg, 0.153 mmol) was dissolved in EtOH (2 mL), and thiourea (46.6 mg, 0.612 mmol) and formic acid (1 drop) were successively added before heating at 80ºC for 2 hrs. The reaction mixture was purified directly by preparative HPLC (acidic method) to give 2-amino-9-(2-phenylpropan-2-yl)-3H-purine-6(9H)-thione (6 mg, 13.8% yield) as a white solid. ^{1}H NMR (400 MHz, DMSO-d_6) δ ppm 11.94 (s, 1H), 8.17 (s, 1H), 7.33 – 7.28 (m, 2H), 7.26 – 7.21 (m, 1H), 7.08 – 7.05 (m, 2H), 6.60 (s, 2H), 2.03 (s, 6H). LCMS: *m/z* 286.2 $[M+H]^+$, Rt = 1.346 min., purity at 254 nm >95%.

General methods and equipment

All commercial reagents and solvents were used without further purification. Analytical thin-layer chromatography was performed on silica gel 60 F-254 plates (E. Merck) and visualized under a UV lamp. 1H NMR spectra were recorded on a Bruker DRX-400. Chemical shifts are

expressed in parts per million (ppm) and referenced to the residual solvent peak. Analytical HPLC-MS was performed on an Agilent MSD mass spectrometer connected to an Agilent 1100 system with method B1090A: column ACE 3 C8 (50 × 3.0 mm); H_2O (+ 0.1% TFA) and MeCN were used as mobile phases at a flow rate of 1 mL/min, with a gradient time of 3.0 min; Preparative HPLC was performed on a Gilson HPLC system: column ACE 5 C8 (150 × 30 mm); H_2O (containing 0.1% TFA) and MeCN were used as mobile phases at a flow rate of 45 mL/min, with a gradient time of 9 min. For HPLC-MS, detection was made by UV using the 180−305 nM range and MS (ESI+). For preparative HPLC, detection was made by UV at 254 or 220 nM. All intermediates and final compounds were assessed to be >95% pure by HPLC-MS analysis, unless stated otherwise.

Protein production

Full-length NUDT15 wild-type and R139C were cloned, expressed, and purified as described previously[16]. Wild-type and L713F PARP1 catalytic domains were also expressed and purified as before[18].

Differential scanning fluorimetry (DSF)

Protein unfolding was detected by differential scanning fluorimetry (DSF[59]). For NUDT15 experiments, 4 μM NUDT15 wild-type or R139C protein were added to 5x SYPRO Orange (ThermoFisher Scientific) in assay buffer (50 mM Tris-HCl, pH 8.0, 100 mM NaCl, 25 mM $NaPO_4$, 5 mM $MgCl_2$) in the presence of DMSO (1% final v/v), 50 μM NSC56456, or 50 μM TH8228. A CFX96 Touch Real-Time PCR Detection System (Bio-Rad) was used to increase the temperature from 25°C to 95°C in 1°C/min increments, and fluorescence intensity was measured at each step. The melting temperature (T_m) was calculated by CFX Manager Software based on minima from the negative first derivative of the melt curve (Bio-Rad).

For PARP1 experiments, the wild-type catalytic domain (5 μM) or the L713F catalytic domain (5 μM) was incubated with PARPi (250 μM) or DMSO control in 25 mM HEPES, pH 8.0, 150 mM NaCl, 0.1 mM TCEP, 1 mM EDTA and 12.5% DMSO. The experiments were performed as previously described[18] using 5x SYPRO Orange (ThermoFisher Scientific) and a Lightcycler 480 (Roche Life Science). The melting temperature (T_m) was calculated based on the minima from the negative first derivative of the melt curve.

Enzyme-coupled malachite green assay

The enzyme-coupled malachite green assay for NUDT15 was performed as previously described[31]. Compounds were dispensed by an Echo Acoustic Liquid Handler to generate final concentrations ranging from 1.69 nM to 100 µM. Purified, wild-type NUDT15 (8 nM) and pyrophosphatase (0.2 u/mL) were combined in assay buffer (100 mM Tris-Acetate, pH 8.0, 40 mM NaCl, 10 mM MgAc, 1 mM DTT, and 0.005% Tween-20) and incubated for 10 minutes at room temperature. Negative controls were samples incubated without NUDT15 protein. Then, 100 µM dGTP (NUDT15 substrate) was added prior to a 15-minute incubation. A malachite green working solution (3.2 mM malachite green carbinol hydrochloride [Sigma Aldrich] in 3M H_2SO_4 complemented with a final concentration of 1.5% ammonium molybdate and 0.17% Tween-20) was then added and followed by an additional 15-minute incubation prior to measuring absorbance at 630 nm on a Hidex Sense microplate reader.

NUDT15-NSC56456 co-crystallization and structure determination

Full length NUDT15 (15 mg/ml) was prepared in sample buffer containing 20 mM HEPES, pH 7.5, 300 mM NaCl, 10% Glycerol, and 2 mM TCEP in the presence of 5 mM NSC56456 dissolved in DMSO. Sitting drop vapour diffusion was performed at 4°C and NUDT15 was mixed with reservoir solution (0.1 M Tris pH 8.5, 0.2M sodium acetate, 30% PEG 4000) in a 1:3 protein/reservoir ratio. Diffraction-quality crystals appeared in the first week, were extracted quickly without additional cryoprotectant, and flash frozen in liquid nitrogen. Data collection was performed at beam line 14.1 at BESSY, Germany, at 100 K and wavelength 0.9184 Å. Data reduction and processing were carried out using DIALS and AIMLESS from the CCP4 software package[60-64]. The structure was solved by molecular replacement of the template structure file with PDB ID 5BON using Phaser6[65] followed by iterative building cycles using the Refine program in Phenix[66]. TLS parameters were determined using the TLSMD webserver[67]. The structure was further validated using PDB_REDO[68] and deposited under PDBID: 7NR6. Relevant statistics are found in **Table S1**.

Cloning

Procedure

3xHA-tagged wild-type and R139C NUDT15[16], as well as V5-tagged wild-type and G48E p18 MTH1[17], lentiviral expression constructs were previously established in pINDUCER20 (a gift from Stephen Elledge (Addgene plasmid # 44012)[69]. GFP-PARP1 was transferred into pINDUCER20 *via* SalI/NotI ligation into pENTR4-N-GFP from pEGFP-C3-PARP1[70]. PARP1 L713F was subcloned from pET28-PARP1 L713F[18] into pENTR1a-C-GFP by flanking SalI/NotI restriction sites and subsequently transferred to pINDUCER20, pCW57.1 (a gift from David Root; Addgene plasmid # 41393), or pLenti CMV Blast DEST (706-1), which was a gift from Eric Campeau & Paul Kaufman (Addgene plasmid # 17451)[71]. To generate pENTR1a-C-nLuc, nanoLuc (gBlock, IDT DNA) was subcloned into pENTR1a by flanking XbaI/XhoI restriction sites. PARP1 L713F was then subcloned into pENTR1a-C-nLuc by flanking SalI/NotI restriction sites prior to transferring into pINDUCER20, pCW57.1, or pLenti CMV blast. mCherry was subcloned from H2B-mCherry (a gift from Robert Benezra; Addgene plasmid # 20972)[72] into pENTR1a by flanking XhoI/XbaI sites prior to transferring to pLenti CMV Blast. Codon-optimized akaLuc[47] was subcloned from pEX-A258-akaLuc (Eurofins) into pENTR4 by flanking NcoI/SalI sites and transferred to pLenti CMV Blast, as before. All subcloning into entry vectors was validated by automated sequencing, while shuttling into destination vectors was performed with Gateway LR Clonase II (ThermoFisher Scientific) and positive clones were confirmed by colony PCR.

Plasmids, primers, and synthetic DNA

All primers and custom vectors were ordered from Eurofins Genomics. gBlock fragments were ordered from IDT. Other plasmids, unless developed in-house, were purchased from Addgene. The sources and sequences of all nucleic acids used in this study are summarized in **Table S2**.

Lentivirus production and transduction

Lentiviral production was performed following transfection of third generation lentiviral packing vectors by calcium phosphate precipitation. pINDUCER20, pCW57.1, or pLenti CMV Blast lentiviral constructs were co-transfected with lentiviral packaging vectors (Gag-Pol, Rev,

and VSV-G envelope) into subconfluent HEK293T cells. Viral particles were harvested at 48- and 72-hours post-transfection, and target cells were transduced at 1:1 dilution of lentivirus and fresh, complete medium in the presence of polybrene (8 µg/mL). Forty-eight hours post-transduction, target cells were re-plated at low density in the presence of G418/neomycin (Sigma-Aldrich, 400 µg/mL for six days; pINDUCER20), puromycin (Sigma-Aldrich, 1 µg/mL for three days; pCW57.1), or blasticidin (Sigma-Aldrich, 5 µg/mL for four days; pLenti CMV Blast) that was replenished at three-day intervals. HCT116 pCW57.1-PARP1 L713F-nLuc cells were selected with 10 µg/mL puromycin over four days to enrich for high transductants.

Reverse transcription quantitative PCR (RT-qPCR)

U-2 OS or HCT116 cells were plated at 40,000 cells/well in 12-well plates in the absence or presence of 1 µg/mL DOX. The following day, DMSO control or indicated inhibitor was added to the cells before harvesting with TRIzol (Thermo Fisher Scientific). RNA was purified with the Direct-zol RNA MiniPrep kit (Zymo Research) according to the manufacturer's instructions and quantified by NanoDrop (Thermo Fisher Scientific). cDNA was then generated with the iScript cDNA Synthesis Kit (Bio-Rad) according to the manufacturer's instructions. qPCR was performed with 2.5 ng cDNA per sample and iTaq Universal SYBR Green Supermix (Bio-Rad) using a Bio-Rad CFX96 Real-Time PCR Detection System. Relative quantity of target genes was calculated using the ΔΔCt method *via* normalization to GAPDH and β-actin or 18s and GAPDH. All qPCR primers are listed in **Table S2**.

Western blotting

Cells were plated and treated as described. At the termination of the experiment, cells were harvested and lysed directly in 1x Laemmli buffer. Following heating for 5 minutes at 95°C, the samples were homogenized by sonication and either directly loaded for electrophoresis or frozen at -80°C for later use. Protein samples were separated on 4-20% gradient Mini-PROTEAN gels (Bio-Rad) or TruPAGE gels (Sigma) prior to transferring onto 0.2 µm nitrocellulose with a Trans-Blot Turbo Transfer System (Bio-Rad). After blocking with LI-COR Blocking Buffer (TBS; LI-COR) for 1 hour at room temperature, primary antibodies were added at the following concentrations in 1:1 LI-COR Blocking Buffer and TBS + 0.05% Tween-20 at 4°C overnight: anti-HA probe (mouse monoclonal, 1:500), anti-GFP (rabbit polyclonal or mouse monoclonal, 1:500),

anti-mCherry (rabbit polyclonal, 1:2000), anti-PARP1 (mouse monoclonal, 1:500), anti-SOD1 (mouse monoclonal, 1:500), anti-CHK1 (mouse monoclonal, 1:1000), anti-p-CHK1 Ser345 (rabbit polyclonal, 1:1000), anti-NUDT15 (rabbit polyclonal, 1:1000), anti-V5 tag (mouse monoclonal, 1:500), anti-NUDT5 (rabbit polyclonal, 1:1000), anti-MTH1 (rabbit polyclonal, 1:500), anti-p-Histone H3 Ser10 (rabbit polyclonal, 1:1000), and anti-γH2A.X (mouse monoclonal, 1:1000). LI-COR secondary antibodies were diluted in 1:1 LI-COR Blocking Buffer (TBS) and TBS + 0.05% Tween-20 at (1:10,000) prior to incubating at room temperature for 1 hour. Blots were imaged with a LI-COR Odyssey Fc and analyzed using Image Studio Software (LI-COR). All uncropped blots with crop marks denoted are available in **Supplementary Fig. 10**.

Qualitative live cell fluorescence microscopy

To initially test GFP PARP1 biosensors in live cells, U-2 OS pINDUCER20-PARP1 L713F-GFP or HCT116 pLenti CMV Blast-PARP1 L713F-GFP/pLenti CMV Blast-mCherry cells were plated in the absence or presence of 1 µg/mL DOX. Where indicated, PARPi were added the following day for 24 to 48 hours. 5 µM MG-132, 100 nM bafilomycin A1, or a combination of both was added for 6 hours prior to imaging with either a ZOE Fluorescent Cell Imager (Bio-Rad) or EVOS FL Cell Imaging System (Thermo Fisher Scientific) at 10, 20, or 40x magnification.

High-content fluorescence microscopy

For NUDT15 R139C experiments in HCT116 3-6 cells, 750 cells were plated in black, clear bottom 96-well plates (BD Falcon) on day 0 in the absence or presence of 1 µg/mL DOX in a volume of 80 µL complete medium. The following day, the appropriate concentrations of inhibitors were added in 10 µL complete medium (3% DMSO v/v). After a 3-hour pre-incubation, either 6TG or equivalent volumes of DMSO were added to the cells in 10 µL complete medium for an additional 72 hours (final DMSO 0.3% v/v). Cells were then fixed with 4% paraformaldehyde (PFA) in PBS for 15 minutes, permeabilized with 0.3% Triton-X100 in PBS for 10 minutes, and then blocked with 3% bovine serum albumin (BSA) in PBS for 1 hour. Anti-HA (1:500) and anti-γH2A.X (rabbit, 1:1000) antibodies were incubated overnight at 4ºC in 3% BSA/PBS. The next day, the cells were washed three times (PBS, PBS+0.05% Tween-20, and then PBS again) before incubation with Alexa Fluor 647 donkey anti-mouse (1:1000) and Alexa Fluor 488 goat anti-rabbit (1:1000) secondary antibodies for 1 hour at room temperature. Following

another round of washes, the cells were counterstained with Hoechst 33342 (1 μg/mL in PBS) for 10 minutes prior to imaging.

For PARP L713F experiments in live U-2 OS cells, 1000 cells were plated in black, clear bottom 96-well plates (BD Falcon) on day 0 in the absence or presence of 1 μg/mL DOX in a volume of 90 μL complete medium. The following day inhibitors were added to their indicated final concentrations in 10 μL of complete medium (final DMSO 0.1% or 1% [3-AB] v/v). After 24 hours, cell-permeable Hoechst 33342 was added to a final concentration of 1 μg/mL for 20 minutes prior to imaging. In instances where cells were fixed, the same set-up and fixation protocol was used as above. Primary antibodies were anti-GFP (mouse monoclonal, 1:300) combined with anti-p-CHK1 Ser345 (rabbit monoclonal, 1:300) or anti-GFP (rabbit polyclonal, 1:300) with anti-γH2A.X (mouse monoclonal, 1:1000). Anti-mouse Alexa Fluor 488 and anti-rabbit Alexa Fluor 647 (GFP mouse and p-CHK1 rabbit) or anti-rabbit Alexa Fluor 488 and anti-mouse Alexa Fluor 647 (GFP rabbit and γH2A.X mouse) were all used at 1:1000 dilutions.

In all cases, imaging was performed on an ImageXpress Micro high-content microscope (Molecular Devices) at 10x magnification (20x for fixed cells stained with anti-γH2A.X). For live-cell imaging, the microscope temperature, humidity, and CO_2 environment controller module were used to maintain cell ambient conditions. Image analysis was then performed with CellProfiler software (Broad Institute), and GraphPad Prism was subsequently used for plotting of data points.

Confocal microscopy, FRAP, and microirradiation

Photobleaching and microirradiation microscopy experiments were carried out with a Zeiss LSM780 confocal laser scanning microscope, equipped with a UV-transmitting Plan-Apochromat 40x/1.30 Oil DIC M27 objective as previously described[73]. U-2 OS cells stably expressing GFP-PARP1 WT or PARP1 L713F-GFP were incubated in phenol-red free media containing DMSO, 5 μM olaparib or 0.5 μM talazoparib for indicated time periods. Cells were transferred to the microscope and eGFP was excited with a 488 nm Ar laser. The microscope was equipped with a heated environmental chamber set to 37°C.

Microirradiation was carried out using either the FRAP module of the ZEISS ZEN software or the tile scanning mode. Cells were pre-sensitized before microirradiation by incubation in medium containing 10 μg/mL Hoechst 33342 for 10 min. For inducing DNA damage with the FRAP module, a 10-pixel diameter spot within the nucleus was irradiated with a 405nm diode

laser set to 100% power. Before and after microirradiation, confocal image series of one mid z-section were recorded at 2 second intervals (typically 6 pre-irradiation and 120 post-irradiation frames). For evaluation of the recruitment kinetics, fluorescence intensities at the irradiated region were corrected for background and for total nuclear loss of fluorescence over the time course and normalized to the pre-irradiation value. For the quantitative evaluation of microirradiation experiments, data of at least 20 nuclei from two independent experiments were averaged and the mean curve and the standard error of the mean calculated and displayed using Microsoft Excel software and GraphPad software.

For DNA damage induction followed by immunofluorescence staining, cells were seeded on µ-Grid (35 mm with Grid, ibidi) dishes and sensitized with Hoechst 33342 (10 µg/mL, 10 minutes). Laser microirradiation was performed using the tile scan mode (3x3 tiles, image size 128x128, scan speed 177.32 µs, every 7th line scanned, 405 nm laser set to 70%), as previously described[74]. After indicated time periods, cells were fixed in 4% paraformaldehyde and permeabilized with 0.5% Triton X-100. Unspecific binding was blocked by incubation in PBS/4% BSA before staining with respective primary antibodies (pan-ADP-ribose binding reagent, 1:1000; γH2A.X, 1:1000). Primary antibodies were detected using secondary antibodies (diluted 1:500-1:1000 in PBS/4% BSA) conjugated to Alexa Fluor 568 or 647 (Thermo Fisher Scientific). Cells were counterstained with DAPI and kept in PBS until images were taken with the LSM780 microscope.

For FRAP analysis, half of the nucleus was marked using the regions tool of the ZEN software (ZEN, Zeiss, Germany) and photobleached with the 488 nm laser set to maximum power at 100% transmission using 5 iterations at scan speed 8 (5 µs). Before and after bleaching, confocal image series were recorded with the following settings: 500 ms time intervals (20 prebleach and 200 postbleach frames), frame size 256x256 pixels, 170 nm pixel size, bidirectional scanning and a pinhole setting of 2.52 airy units. Mean fluorescence intensities of the bleached region were corrected for background and for total nuclear loss of fluorescence over time. For the quantitative evaluation of photobleaching experiments, data of at least 45 nuclei from five independent experiments were averaged and the mean curve, the standard error of the mean (s.e.m.), halftime of recovery (t½) and mobile fraction (Mf) calculated and displayed using Microsoft Excel software and GraphPad Prism.

Flow cytometry

MTH1 G48E studies

For MTH1 studies, 400,000 U-2 OS V5-MTH1 G48E clone #6 cells were plated in T25 flasks in the presence of 1 µg/mL DOX on day 0. The following morning (day 1), the cells were then treated with DMSO (0.01% v/v final concentration), 2.5 µM TH588, or 1 µM AZ19 for 24 hours. On the morning of day 2, the cells were harvested by trypsinization and pooling of culture medium, as well as PBS washes (to ensure collection of dead and mitotic cells). Following a wash with PBS, the cells were fixed with 4% PFA in PBS for 15 minutes, washed once with 1% BSA/PBS, then permeabilized with saponin buffer (0.1% saponin in 1% BSA/PBS) on ice for 30 minutes. The cells were then stained with anti-V5 (mouse monoclonal, 1:300) and anti-p-HH3 Ser10 (rabbit polyclonal, 1:500) antibodies diluted in saponin buffer overnight at 4ºC. Next, the cells were washed twice with saponin buffer prior to incubation with donkey anti-mouse Alexa Fluor 647 and donkey anti-rabbit Alexa Fluor 488 antibodies (1:1000 in saponin buffer) for 30 minutes at 37ºC. Following two additional washes with saponin buffer, the cells were incubated with 0.1 mg/mL RNase A (Thermo Fisher Scientific) and 10 µg/mL Hoechst 33342 for 15 minutes at room temperature in 1% BSA/PBS. Control V5-MTH1 G48E cells were also used for singlet antibody controls (one for V5 and one for p-HH3 Ser10). The cells were then analyzed by flow cytometry on a Navios EX flow cytometer (Beckman Coulter) using Navios System Software for acquisition (V5-Alexa Fluor 647: FL6, p-HH3 Ser10-Alexa Fluor 488: FL1, Hoechst: FL9). Analysis and final gating of cell populations was performed with Kaluza Analysis Software (Beckman Coulter; see **Supplementary Fig. 11a**). In addition, FlowJo (Bectin Dickenson) was used to export raw, per-event values for each parameter for subsequent plotting and analysis in GraphPad Prism.

PARP1 L713F studies

PARP1 experiments were performed with live U-2 OS pINDUCER20-PARP1 L713F-GFP #5/pLenti CMV Blast-mCherry or HCT116 pLenti CMV Blast-PARP1 L713F-GFP/pLenti CMV Blast-mCherry cells. Briefly, 200,000 cells were plated in T25 flasks (in the presence of 1 µg/mL DOX for U-2 OS cells). The following day, varying concentrations of veliparib/niraparib or an equivalent volume of DMSO was added to the cells prior to harvesting 24 hours later. Trypsinized cells were quenched with complete medium, pelleted at 400 x *g* for 5 minutes, washed by

resuspending in sterile PBS/10% FBS, centrifuged again, and then transferred to 5 mL flow cytometry tubes *via* a 40 µm strainer cap (BD Falcon) in 500 µL sterile PBS/5% FBS. The samples were then analyzed on a BD Accuri C6 flow cytometer (Bectin Dickenson) with BD Accuri C6 software (GFP – PARP1 L713F stabilization, mCherry – fluorescence normalization). Unstained parental U-2 OS or U-2 OS pINDUCER20-L713F cells without DOX were used to establish final gating with FlowJo (Bectin Dickenson; **Supplementary Fig. 11b**), which was used for both cell lines.

In vitro luciferase assays

nLuc assays

For nLuc luciferase assays with U-2 OS PARP1 pINDUCER20-PARP1 L713F-nLuc cells, 1,000 cells per well were plated in white 96-well plates (Greiner) in complete medium and in the absence or presence of 1 µg/mL DOX. The following day, the medium was changed to FluoroBrite DMEM phenol red-free medium (Thermo Fisher Scientific) in the presence of DMSO or PARP inhibitor (fresh DOX was also added where necessary), and the cells were incubated for another 24 hours. nanoLuc signal was assessed using the Nano-Glo Luciferase Assay System (Promega) according to the manufacturer's instructions and the signal was quantified on a Hidex Sense plate reader with 1-second reads and an open filter setting. Readings were made every 3 minutes for up to 30 minutes following the addition of the lysis reagent.

For sensitivity measurements, U-2 OS cells were plated at serial dilutions ranging from 12 to 1,500 cells in white 96-well plates (Greiner) in complete medium and the presence of 1 µg/mL DOX. The medium was changed to FluoroBrite DMEM with DOX the following day and either DMSO or 2 µM veliparib were added to the cells for an additional 24 hours, before assaying by Nano-Glo kit with a Hidex Sense plate reader and an open filter. Signal-to-noise (S/N; S/N = [mean signal–mean background]/standard deviation of background – $[\mu_S-\mu_B]/\sigma_B$) and signal-to-background (S/B; S/B = mean signal/mean background – μ_S/μ_B) were calculated for each number of cells plated[48].

For dose response experiments with HCT116 pCW57.1-PARP1 L713F-nLuc cells, 4,000 cells were plated in white 96-well plates (Greiner) in the absence or presence of 1 µg/mL DOX. The following day the medium was changed to complete FluoroBrite DMEM containing talazoparib (max conc. 10 µM), 3-AB (max conc. 1 mM), or iniparib (max conc. 20 µM) for 24

hours. The following day the medium was changed to furimazine-containing FluoroBrite (1:200 dilution from Nano-Glo kit) and immediately imaged with a CLARIOStar microplate reader (BMG LABTECH) with an open filter followed by a nLuc filter (470 ± 40 nm) both with spiral averaging feature.

Combined nLuc and akaLuc assays

Luminescence spectral profiling for both nLuc and akaLuc was determined by pre-treatment of HCT116 pCW57.1-PARP1 L713F-nLuc/pLenti-CMV-blast-akaLuc cells with 1 µg/mL DOX for 24 hours and 1 µM veliparib for an additional 24 hours. nLuc spectral profiling was performed immediately after the addition of a 1:200 dilution of Nano-Glo substrate in FluoroBrite DMEM, while the akaLuc spectrum was determined with 200 µM akaLumine HCl in FluoroBrite DMEM. Spectral scanning was determined on a CLARIOstar microplate reader on the spiral averaging setting.

For testing akaLuc luminescence and cross-reactivity with nLuc signal, HCT116 pCW57.1-PARP1 L713F-nLuc/pLenti-CMV-blast-akaLuc cells were plated at 4,000 cells per well unless otherwise stated and subjected to several different conditions. While testing akaLuc alone, luminescence signals were first established by comparison to parental HCT116 cells. The day after plating, the medium was changed to complete FluoroBrite DMEM with 200 µM akaLumine HCl and immediately measured on a CLARIOStar microplate reader with an open filter and spiral averaging feature.

To determine akaLuc tolerance to detergent-mediated lytic conditions, cells were prepared for detection with 200 µM akaLumine HCl diluted in Nano-Glo lysis reagent (according to the lysis conditions described by the manufacturer) or 100 or 200 µM akaLumine HCl diluted in complete FluoroBrite DMEM medium before luminescence detection on an open filter and spiral averaging feature.

For experiments testing simultaneous detection of nLuc and akaLuc signals, the cells were plated in complete medium supplemented with 1 µg/mL DOX. The following day, the cells were supplemented with 2 µM veliparib for an additional 24 hours. Just prior to imaging, the medium was replaced with complete FluoroBrite DMEM medium supplemented with 200 µM akaLumine HCl and furimazine (1:200 dilution) and immediately detected sequentially on an nLuc filter (470 ± 40 nm) and an akaLuc filter setting (650 ± 40 nm) using the spiral averaging feature.

For sequential reading of akaLuc signal followed by nLuc signal, HCT116 pCW57.1-PARP1 L713F-nLuc/pLenti-CMV-blast-akaLuc cells were plated in complete medium in the absence or presence of 1 µg/mL DOX (or not at all for HCT116 pLenti-CMV-blast-PARP1 L713F-nLuc/pLenti-CMV-blast-akaLuc cells used for animal experiments) prior to incubation with indicated concentrations of PARPi for 24 hours. On the day of imaging, the medium was first changed to complete FluoroBrite DMEM with 200 µM akaLumine HCl and immediately imaged with an open filter and spiral averaging feature. Following a wash with FluoroBrite DMEM, the medium was changed again to FluoroBrite DMEM with a 1:200 dilution of furimazine and immediately imaged with an open filter and spiral averaging feature. nLuc signal was then normalized to akaLuc signal to obtain relative signal values and then normalized to DMSO-treated (in some cases, +DOX) controls to give fold change.

Time- and target concentration-dependence of L713F-nLuc stabilization

Time-dependent stabilization of PARP1 L713F-nLuc by PARPi was determined with HCT116 pCW57.1-PARP1 L713F-nLuc/pLenti CMV Blast-akaLuc cells plated at 4,000 per well in the absence or presence of 1 µg/mL DOX. The following day, veliparib was added at different concentrations for 1, 8, or 24 hours prior to sequential akaLuc and nLuc detection as before. Fold nLuc signal was calculated by normalization of nLuc intensity to akaLuc intensity and relative to DMSO + DOX treatment. The influence of PARP1 L713F-nLuc target abundance on stabilization by PARPi was determined as above, but cells were pre-treated with 10, 100, 333, or 1 µg/mL DOX overnight followed by 24-hr treatment with veliparib at different concentrations. Luciferase activity signals were again detected sequentially and nLuc intensity was normalized to akaLuc intensity and set relative to DMSO + DOX readings.

In vivo target engagement in tumor xenografts

Ethical statement

Work was performed in accordance with EU (European Union) and Swedish regulations for ethical animal experimentation under Karolinska Institutet permit no. 5718-2019.

Establishment of PARP1 L713F-GFP/mCherry tumor xenografts and treatment with PARPi

HCT116 pLenti CMV Blast-PARP1 L713F-GFP/pLenti CMV Blast-mCherry cells were injected subcutaneously into the flanks of BALB/cAnNCrl nude mice (strain code: 194 [homozygous], Charles River Labs) at $2x10^6$ cells in 100 µL PBS. Once the tumors reached approximately 200 mm^3 in size, mice were systemically administered vehicle, 15 mg/kg, or 60 mg/kg niraparib formulated in 0.5% methylcellulose (Sigma) by oral gavage once daily (qd) for two days. On day three, the tumors were harvested and sub-divided for downstream analysis as follows: one half was formaldehyde-fixed and paraffin-embedded for sectioning and immunofluorescence analysis, one quarter was snap frozen for western blot analysis, and one quarter was immediately dissociated for live cell flow cytometry analysis.

Tumor dissociation and flow cytometry

Dissociation of excised subcutaneous HCT116 L713F-GFP/mCherry tumors was performed similarly to previously reported methods[75]. Briefly, approximately 60-80 mm^3 of tumor tissue was finely minced with a sterile scalpel and dissociated for 1 hour at 37°C with shaking in 9 mL of an enzyme solution containing 1 mg/mL collagenase D (Sigma) and 100 ng/mL DNAse I (≥40 U/mL final; Sigma) in McCoy's 5a GlutaMAX without additives. For the final 5 minutes of the incubation period, 1 mL TrypLE Express was added to each tube. Digestive enzymes were deactivated by the addition of 3 mL McCoy's 5a medium containing 10% FBS and the cell suspension was sieved through a 40 µm strainer (Corning), followed by an additional rinse with 2 mL McCoy's/10% FBS. The cells were pelleted by centrifugation at 400 x *g* for 5 minutes and washed by resuspension in sterile PBS/10% FBS. After centrifugation, the cell pellet was resuspended in 1 mL sterile PBS/5% FBS and transferred to a 5 mL flow cytometry tube *via* a 40 µm strainer cap (BD Falcon). Viability of the final samples was between 30-35% by trypan blue exclusion. Tumor suspensions were assayed on a BD Accuri C6 (Bectin Dickenson) with identical gating strategy for cultured HCT116 GFP/mCherry cells (**Supplementary Fig. 11b**). Relative L713F-GFP was determined by normalizing median GFP intensity to median mCherry intensity for each tumor.

Western blotting

Excised tumor samples were immediately snap frozen on dry ice and stored at -80ºC until use. In preparation for lysis, tumor masses were then pulverized with a mortar and pestle in liquid nitrogen prior to lysis in RIPA buffer and clarification of proteins by centrifugation. Following protein concentration measurements by BCA assay, equal concentrations of tumor lysate were prepared for western blotting, as above. Primary antibodies used were anti-GFP (mouse; 1:500), anti-mCherry (rabbit; 1:2000), and anti-β-actin (mouse; 1:5000).

Sectioning, mounting, and immunohistochemistry

Following excision, tumors were fixed in 4% PFA/PBS for one day and then submerged in 70% ethanol. Paraffinization, sectioning, and mounting of tumors was performed in the Pathology Core Facility at Karolinska Institutet Huddinge campus.

In preparation for immunofluorescence, the sections were deparaffinized and rehydrated with the following steps: 1. Xylene: 2 x 3 minutes, 2. Xylene/100% ethanol (1:1): 3 minutes, 3. 100% ethanol: 2 x 3 minutes, 4. 95% ethanol: 3 minutes, 5. 70% ethanol: 3 minutes, 6. 50% ethanol: 3 minutes, 7. Rinse with cold tap water. Following deparaffinization, antigen retrieval was carried out with citric acid buffer in a standard pressure cooker made for slides. The slides were then washed 2 x 5 minutes with TBS/0.025% Triton X-100 under gentle agitation, followed by blocking in 2% BSA/TBS for 2 hours at room temperature under high humidity. Anti-GFP primary antibody (1:100, mouse monoclonal, Santa Cruz) was then incubated overnight at 4°C in 2% BSA/TBS. The next day, the slides were washed 3 x 5 minutes in TBS/0.025% Triton X-100 with gentle agitation. Following washing, donkey anti-mouse Alexa Fluor 555 secondary antibody (1:1000 in 2% BSA/TBS) was applied on the slides and incubated at room temperature for 1 hour. The slides were again washed under gentle agitation 3 x 5 minutes in TBS, followed by rinsing with distilled water. The sections were counterstained with DAPI (1:1000), rinsed once with distilled water, and mounted with ProLong Gold (Thermo Fisher). Images were taken using a 40x objective on a Zeiss LSM780 confocal laser scanning microscope and processed in Fiji (ImageJ).

Establishment of PARP1 L713F-nLuc/akaLuc tumor xenografts and treatment with PARPi

HCT116 pLenti CMV Blast-PARP1 L713F-nLuc/pLenti CMV Blast-akaLuc cells were injected subcutaneously and treated with vehicle control or 60 mg/kg niraparib as above.

Bioluminescence imaging of PARP1 L713F-nLuc/akaLuc tumors in live animals

akaLuc and nLuc bioluminescence signals were sequentially imaged on an IVIS Spectrum (Perkin Elmer). On day two, the animals were anesthetized by isoflurane gas and 1 mg (3 µmol) akaLumine HCl in 100 µL sterile saline was administered IP prior to immediately imaging to determine tumor akaLuc signals[49]. akaLuc bioluminescence was measured every minute for 20 minutes with the instrument settings of open filter, medium binning, 60 second exposure time, and f-stop of 1. To ensure metabolic clearance of akaLumine HCl, the following day, 120 µL of fluorofurimazine/P-407 solution (1 µmol) was administered IP for detection of L713F-nLuc[49], and the mice were again immediately imaged on an IVIS Spectrum with measurements every minute over 20 minutes. Instrument settings were the same as above. Results are presented as radiance (p/sec/cm^2/sr) or total flux (photons/sec). Relative L713F-nLuc luminescence was calculated by normalization to akaLuc signal.

Ex vivo bioluminescence measurements

Following clearance of fluorofurimazine on day three of niraparib treatment, tumors were excised from the mice prior to sectioning with a sterile scalpel, and a quarter of each tumor was transferred to a well in a white, 96-well plate (Greiner). Tumor masses were gently flattened with sterile Dounce homogenizer plungers to spread tissue evenly in the well and submerged in 200 µL FluoroBrite DMEM containing 200 µM AkaLumine HCl. Immediately after addition of Akalumine, tumor akaLuc luminescence was measured with a CLARIOStar microplate reader on an open filter with the spiral averaging feature. The AkaLumine was then removed, and tumors were briefly washed with FluoroBrite DMEM prior to submerging in 200 µL furimazine-FluoroBrite (diluted 1:200 from the Promega Nano-Glo kit). L713F-nLuc signals were then immediately measured using nLuc-specific filter settings (470 ± 40 nm). To determine relative L713F-nLuc luminescence, signals were normalized to akaLuc readings and set relative to the vehicle control tumors.

<u>Statistical analyses and data transformation</u>

All graphing and statistical analyses were performed using GraphPad Prism V9. Saturation curve fitting was performed using the [agonist] vs response four parameter variable slope model in GraphPad Prism. Specific post-hoc tests, variations, and statistical significances for relevant

experiments are described within individual figure legends. In some instances, raw data were transformed to simplify graphical visualization. Specifically, fluorescence values in **Fig. 2i**; **Fig. 3h** and **j**; **Supplementary Fig. 4a** and **c**; GFP in **Fig. 4e-g**; **Supplementary Fig. 5a, c, e**, and **g**; **Extended Data Fig. 6b, c, e, g, h**, and **j**; **Supplementary Fig. 6a** and b; and **Supplementary Fig. 7a** and **b** were multiplied by a factor of 100, whereas Hoechst fluorescence values in **Fig. 2f** and **i** were divided by a factor of 100,000.

References

1. Simon, G.M., Niphakis, M.J. & Cravatt, B.F. Determining target engagement in living systems. *Nat Chem Biol* **9**, 200-205 (2013).
2. Bunnage, M.E., Gilbert, A.M., Jones, L.H. & Hett, E.C. Know your target, know your molecule. *Nature Chemical Biology* **11**, 368-372 (2015).
3. Robers, M.B. et al. Quantifying Target Occupancy of Small Molecules Within Living Cells. *Annu Rev Biochem* **89**, 557-581 (2020).
4. Morgan, P. et al. Impact of a five-dimensional framework on R&D productivity at AstraZeneca. *Nat Rev Drug Discov* **17**, 167-181 (2018).
5. Molina, D.M. et al. Monitoring Drug Target Engagement in Cells and Tissues Using the Cellular Thermal Shift Assay. *Science* **341**, 84-87 (2013).
6. Seashore-Ludlow, B., Axelsson, H. & Lundbäck, T. Perspective on CETSA Literature: Toward More Quantitative Data Interpretation. *SLAS Discov* **25**, 118-126 (2020).
7. Seashore-Ludlow, B. et al. Quantitative Interpretation of Intracellular Drug Binding and Kinetics Using the Cellular Thermal Shift Assay. *Biochemistry* **57**, 6715-6725 (2018).
8. Cimmperman, P. et al. A Quantitative Model of Thermal Stabilization and Destabilization of Proteins by Ligands. *Biophysical Journal* **95**, 3222-3231 (2008).
9. Lee, C., Schwartz, M.P., Prakash, S., Iwakura, M. & Matouschek, A. ATP-dependent proteases degrade their substrates by processively unraveling them from the degradation signal. *Mol Cell* **7**, 627-637 (2001).
10. Hartl, F.U., Bracher, A. & Hayer-Hartl, M. Molecular chaperones in protein folding and proteostasis. *Nature* **475**, 324-332 (2011).
11. Feng, J. et al. A general strategy to construct small molecule biosensors in eukaryotes. *Elife* **4** (2015).
12. Banaszynski, L.A., Chen, L.C., Maynard-Smith, L.A., Ooi, A.G. & Wandless, T.J. A rapid, reversible, and tunable method to regulate protein function in living cells using synthetic small molecules. *Cell* **126**, 995-1004 (2006).
13. Lévy, F., Johnston, J.A. & Varshavsky, A. Analysis of a conditional degradation signal in yeast and mammalian cells. *Eur J Biochem* **259**, 244-252 (1999).

14. Banaszynski, L.A. & Wandless, T.J. Conditional control of protein function. *Chem Biol* **13**, 11-21 (2006).
15. Stein, A., Fowler, D.M., Hartmann-Petersen, R. & Lindorff-Larsen, K. Biophysical and Mechanistic Models for Disease-Causing Protein Variants. *Trends Biochem Sci* **44**, 575-588 (2019).
16. Valerie, N.C.K. et al. NUDT15 Hydrolyzes 6-Thio-DeoxyGTP to Mediate the Anticancer Efficacy of 6-Thioguanine. *Cancer Research* **76**, 5501-5511 (2016).
17. Mur, P. et al. Germline variation in the oxidative DNA repair genes NUDT1 and OGG1 is not associated with hereditary colorectal cancer or polyposis. *Hum Mutat* **39**, 1214-1225 (2018).
18. Langelier, M.F., Planck, J.L., Roy, S. & Pascal, J.M. Structural basis for DNA damage-dependent poly(ADP-ribosyl)ation by human PARP-1. *Science* **336**, 728-732 (2012).
19. Mo, J.Y., Maki, H. & Sekiguchi, M. Hydrolytic elimination of a mutagenic nucleotide, 8-oxodGTP, by human 18-kilodalton protein: sanitization of nucleotide pool. *Proceedings of the National Academy of Sciences* **89**, 11021-11025 (1992).
20. Gad, H. et al. MTH1 inhibition eradicates cancer by preventing sanitation of the dNTP pool. *Nature* **508**, 215-221 (2014).
21. Huber, K.V.M. et al. Stereospecific targeting of MTH1 by (S)-crizotinib as an anticancer strategy. *Nature* **508**, 222-227 (2014).
22. Ellermann, M. et al. Novel Class of Potent and Cellularly Active Inhibitors Devalidates MTH1 as Broad-Spectrum Cancer Target. *ACS Chem Biol* **12**, 1986-1992 (2017).
23. Petrocchi, A. et al. Identification of potent and selective MTH1 inhibitors. *Bioorg Med Chem Lett* **26**, 1503-1507 (2016).
24. Kettle, J.G. et al. Potent and Selective Inhibitors of MTH1 Probe Its Role in Cancer Cell Survival. *J Med Chem* **59**, 2346-2361 (2016).
25. Gul, N. et al. The MTH1 inhibitor TH588 is a microtubule-modulating agent that eliminates cancer cells by activating the mitotic surveillance pathway. *Sci Rep* **9**, 14667 (2019).
26. Patterson, J.C. et al. VISAGE Reveals a Targetable Mitotic Spindle Vulnerability in Cancer Cells. *Cell Syst* **9**, 74-92.e78 (2019).

27. Kawamura, T. et al. Proteomic profiling of small-molecule inhibitors reveals dispensability of MTH1 for cancer cell survival. *Sci Rep* **6**, 26521 (2016).
28. Moriyama, T. et al. NUDT15 polymorphisms alter thiopurine metabolism and hematopoietic toxicity. *Nature Genetics* **48**, 367-373 (2016).
29. Rehling, D. et al. Crystal structures of NUDT15 variants enabled by a potent inhibitor reveal the structural basis for thiopurine sensitivity. *J Biol Chem*, 100568 (2021).
30. Zhang, S.M. et al. NUDT15-mediated hydrolysis limits the efficacy of anti-HCMV drug ganciclovir. *Cell Chem Biol* **28**, 1693-1702.e1696 (2021).
31. Zhang, S.M. et al. Development of a chemical probe against NUDT15. *Nat Chem Biol* **16**, 1120-1128 (2020).
32. Miranda, E.A., Dantzer, F., O'Farrell, M., de Murcia, G. & de Murcia, J.M. Characterisation of a gain-of-function mutant of poly(ADP-ribose) polymerase. *Biochem Biophys Res Commun* **212**, 317-325 (1995).
33. Gibson, B.A. & Kraus, W.L. New insights into the molecular and cellular functions of poly(ADP-ribose) and PARPs. *Nature Reviews Molecular Cell Biology* **13**, 411-424 (2012).
34. Rank, L. et al. Analyzing structure-function relationships of artificial and cancer-associated PARP1 variants by reconstituting TALEN-generated HeLa PARP1 knock-out cells. *Nucleic Acids Res* **44**, 10386-10405 (2016).
35. Dawicki-McKenna, J.M. et al. PARP-1 Activation Requires Local Unfolding of an Autoinhibitory Domain. *Mol Cell* **60**, 755-768 (2015).
36. Murai, J. et al. Trapping of PARP1 and PARP2 by Clinical PARP Inhibitors. *Cancer Res* **72**, 5588-5599 (2012).
37. Maya-Mendoza, A. et al. High speed of fork progression induces DNA replication stress and genomic instability. *Nature* **559**, 279-284 (2018).
38. Zandarashvili, L. et al. Structural basis for allosteric PARP-1 retention on DNA breaks. *Science* **368** (2020).
39. Kam, T.I. et al. Poly(ADP-ribose) drives pathologic α-synuclein neurodegeneration in Parkinson's disease. *Science* **362** (2018).

40. Michelena, J. et al. Analysis of PARP inhibitor toxicity by multidimensional fluorescence microscopy reveals mechanisms of sensitivity and resistance. *Nat Commun* **9**, 2678 (2018).
41. Pommier, Y., O'Connor, M.J. & de Bono, J. Laying a trap to kill cancer cells: PARP inhibitors and their mechanisms of action. *Sci Transl Med* **8**, 362ps317 (2016).
42. Mateo, J., Ong, M., Tan, D.S.P., Gonzalez, M.A. & de Bono, J.S. Appraising iniparib, the PARP inhibitor that never was—what must we learn? *Nature Reviews Clinical Oncology* **10**, 688-696 (2013).
43. Schwartz, J.L., Morgan, W.F., Kapp, L.N. & Wolff, S. Effects of 3-aminobenzamide on DNA synthesis and cell cycle progression in Chinese hamster ovary cells. *Exp Cell Res* **143**, 377-382 (1983).
44. Sun, K. et al. A comparative pharmacokinetic study of PARP inhibitors demonstrates favorable properties for niraparib efficacy in preclinical tumor models. *Oncotarget* **9**, 37080-37096 (2018).
45. Baker, J.H. et al. Targeting the tumour vasculature: exploitation of low oxygenation and sensitivity to NOS inhibition by treatment with a hypoxic cytotoxin. *PLoS One* **8**, e76832 (2013).
46. Fior, R. et al. Single-cell functional and chemosensitive profiling of combinatorial colorectal therapy in zebrafish xenografts. *Proc Natl Acad Sci U S A* **114**, E8234-E8243 (2017).
47. Iwano, S. et al. Single-cell bioluminescence imaging of deep tissue in freely moving animals. *Science* **359**, 935-939 (2018).
48. Zhang, J.H., Chung, T.D. & Oldenburg, K.R. A Simple Statistical Parameter for Use in Evaluation and Validation of High Throughput Screening Assays. *J Biomol Screen* **4**, 67-73 (1999).
49. Su, Y. et al. Novel NanoLuc substrates enable bright two-population bioluminescence imaging in animals. *Nat Methods* **17**, 852-860 (2020).
50. Zhao, H. et al. Emission spectra of bioluminescent reporters and interaction with mammalian tissue determine the sensitivity of detection in vivo. *J Biomed Opt* **10**, 41210 (2005).

51. Savitski, M.M. et al. Tracking cancer drugs in living cells by thermal profiling of the proteome. *Science* **346**, 1255784 (2014).
52. Lomenick, B. et al. Target identification using drug affinity responsive target stability (DARTS). *Proceedings of the National Academy of Sciences* **106**, 21984-21989 (2009).
53. Cho, K.F. et al. Chaperone mediated detection of small molecule target binding in cells. *Nat Commun* **11**, 465 (2020).
54. Rocklin, G.J. et al. Global analysis of protein folding using massively parallel design, synthesis, and testing. *Science* **357**, 168-175 (2017).
55. Matreyek, K.A. et al. Multiplex assessment of protein variant abundance by massively parallel sequencing. *Nat Genet* **50**, 874-882 (2018).
56. Maynard-Smith, L.A., Chen, L.C., Banaszynski, L.A., Ooi, A.G. & Wandless, T.J. A directed approach for engineering conditional protein stability using biologically silent small molecules. *J Biol Chem* **282**, 24866-24872 (2007).
57. Page, B.D.G. et al. Targeted NUDT5 inhibitors block hormone signaling in breast cancer cells. *Nat Commun* **9**, 250 (2018).
58. Gad, H. et al. MTH1 promotes mitotic progression to avoid oxidative DNA damage in cancer cells. *bioRxiv*, 575290 (2019).
59. Niesen, F.H., Berglund, H. & Vedadi, M. The use of differential scanning fluorimetry to detect ligand interactions that promote protein stability. *Nature Protocols* **2**, 2212-2221 (2007).
60. Evans, P.R. & Murshudov, G.N. How good are my data and what is the resolution? *Acta Crystallogr D Biol Crystallogr* **69**, 1204-1214 (2013).
61. Evans, P. Scaling and assessment of data quality. *Acta Crystallogr D Biol Crystallogr* **62**, 72-82 (2006).
62. Winn, M.D. et al. Overview of the CCP4 suite and current developments. *Acta Crystallogr D Biol Crystallogr* **67**, 235-242 (2011).
63. Winter, G. xia2: an expert system for macromolecular crystallography data reduction. *Journal of Applied Crystallography* **43**, 186-190 (2010).
64. Winter, G. et al. DIALS: implementation and evaluation of a new integration package. *Acta Crystallogr D Struct Biol* **74**, 85-97 (2018).

65. McCoy, A.J. Solving structures of protein complexes by molecular replacement with Phaser. *Acta Crystallogr D Biol Crystallogr* **63**, 32-41 (2007).
66. Adams, P.D. et al. PHENIX: a comprehensive Python-based system for macromolecular structure solution. *Acta Crystallogr D Biol Crystallogr* **66**, 213-221 (2010).
67. Painter, J. & Merritt, E.A. TLSMD web server for the generation of multi-group TLS models. *Journal of Applied Crystallography* **39**, 109-111 (2006).
68. Joosten, R.P., Long, F., Murshudov, G.N. & Perrakis, A. The PDB_REDO server for macromolecular structure model optimization. *IUCrJ* **1**, 213-220 (2014).
69. Meerbrey, K.L. et al. The pINDUCER lentiviral toolkit for inducible RNA interference in vitro and in vivo. *Proceedings of the National Academy of Sciences* **108**, 3665-3670 (2011).
70. Maeda, Y. et al. PARP-2 interacts with TTF-1 and regulates expression of surfactant protein-B. *J Biol Chem* **281**, 9600-9606 (2006).
71. Campeau, E. et al. A Versatile Viral System for Expression and Depletion of Proteins in Mammalian Cells. *PLOS ONE* **4**, e6529 (2009).
72. Nam, H.S. & Benezra, R. High levels of Id1 expression define B1 type adult neural stem cells. *Cell Stem Cell* **5**, 515-526 (2009).
73. Xie, S. et al. Timeless Interacts with PARP-1 to Promote Homologous Recombination Repair. *Mol Cell* **60**, 163-176 (2015).
74. Baldeyron, C., Soria, G., Roche, D., Cook, A.J. & Almouzni, G. HP1alpha recruitment to DNA damage by p150CAF-1 promotes homologous recombination repair. *J Cell Biol* **193**, 81-95 (2011).
75. Wagner, K.D. et al. The Wilms' tumour suppressor Wt1 is a major regulator of tumour angiogenesis and progression. *Nat Commun* **5**, 5852 (2014).
76. Purnell, M.R. & Whish, W.J. Novel inhibitors of poly(ADP-ribose) synthetase. *Biochem J* **185**, 775-777 (1980).
77. Fakan, S., Leduc, Y., Lamarre, D., Brunet, G. & Poirier, G.G. Immunoelectron microscopical distribution of poly(ADP-ribose)polymerase in the mammalian cell nucleus. *Exp Cell Res* **179**, 517-526 (1988).
78. Engbrecht, M. & Mangerich, A. The Nucleolus and PARP1 in Cancer Biology. *Cancers (Basel)* **12** (2020).

79. Haince, J.F. et al. PARP1-dependent kinetics of recruitment of MRE11 and NBS1 proteins to multiple DNA damage sites. *J Biol Chem* **283**, 1197-1208 (2008).

Acknowledgments: The authors thank Promega for providing fluorofurimazine (Thomas Kirkland and Joel Walker); Sean Rudd, Kristoffer Valerie, Thomas Gustafsson, as well as many other colleagues for critical feedback and discussion of the work; the beamline scientists at BESSY II (Berlin, Germany) for help with structural data collection; and the Protein Science Facility (PSF) at Karolinska Institutet and SciLifeLab (http://ki.se/psf).

Funding: Swedish Childhood Cancer Society (TJ2019-0036 – NCKV; PR2016-0101 – TH), Cancer Research KI (Karolinska Institutet) Blue Sky Grant (NCKV), Felix Mindus Contribution to Leukemia Research (2019-01992 – NCKV), Loo and Hans Osterman Foundation (2020-01208 – NCKV), Karolinska Institutet Research Foundation (2020-01685 – NCKV; 2018-01655 – BDGP), Swedish Society for Medical Research (S16-0152 – BDGP), Michael Smith Foundation for Health Research (18292 – BDGP), Canadian Institutes of Health Research (BMA342854 – JMP), European Research Council (TAROX-695376 – TH; 2015-00162 – TH; 2018-03406 – PS), Swedish Pain Relief Foundation (SSF/01-05 – TH), Swedish Cancer Society (21 0352 PT – NV; CAN2018/0658 – TH; 201287 – PS), Torsten and Ragnar Söderberg Foundation (TH), Alfred Österlund Foundation (PS), Hållsten Foundation (MA), SciLifeLab Technology Development Project Grant (MA)

Author contributions: Conceptualization (NCKV, BDGP, MA), Methodology (NCKV), Investigation (NCKV [lead], KS, OM, SMZ, AR, MFL, DR, AT, MD, PW, IA, SA, JB, LB, BDGP), Resources (PS, JMP, TH, BDGP, MA), Writing – original draft (NCKV [lead], BDGP, MA), Writing – review & editing: (NCKV [lead], KS, OM, SMZ, AR, MFL, DR, AT, MD, PW, IA, SA, JB, LB, PS, JMP, TH, BDGP, MA), Visualization: (NCKV [lead], KS, OM, DR), Supervision (NCKV [lead], PS, JMP, TH, BDGP, MA), Project administration (NCKV), Funding acquisition (NCKV, PS, JMP, TH, BDGP, MA)

Competing interests: NCKV, BDGP, and MA are inventors on a patent application describing CeTEAM and its uses. The remaining authors declare no competing interests.

Data and materials availability: All data is available in the main text or the supplementary materials. The NUDT15-NSC56456 co-crystal structure was deposited to the RCSB Protein Data Bank under PDBID: 7NR6.

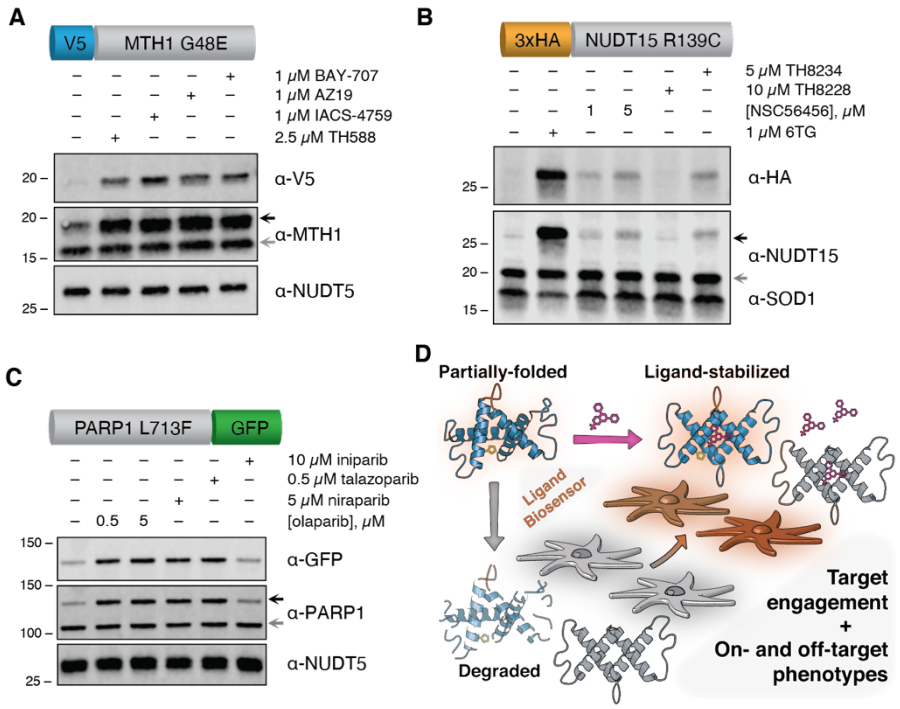

Fig. 1. CeTEAM is predicated on stability-dependent biosensors to measure drug binding. a, U-2 OS V5-MTH1 G48E cells were treated with the indicated MTH1 inhibitors for 24 hours. **b**, HCT116 3-6 3xHA-NUDT15 R139C cells were incubated with the indicated molecules for 72 hours. **c**, U-2 OS PARP1 L713F-GFP cells were treated with PARP inhibitors for 24 hours. **d**, A schematic description of CeTEAM. Stability-dependent drug biosensors (blue) accumulate in the presence of binding ligand (pink) and can be detected by protein fusion tags (orange) as a measure of target engagement. Endogenous target protein (grey) and physiological conditions enable phenotypic multiplexing and discerning of on- from off-target effects of test compounds.

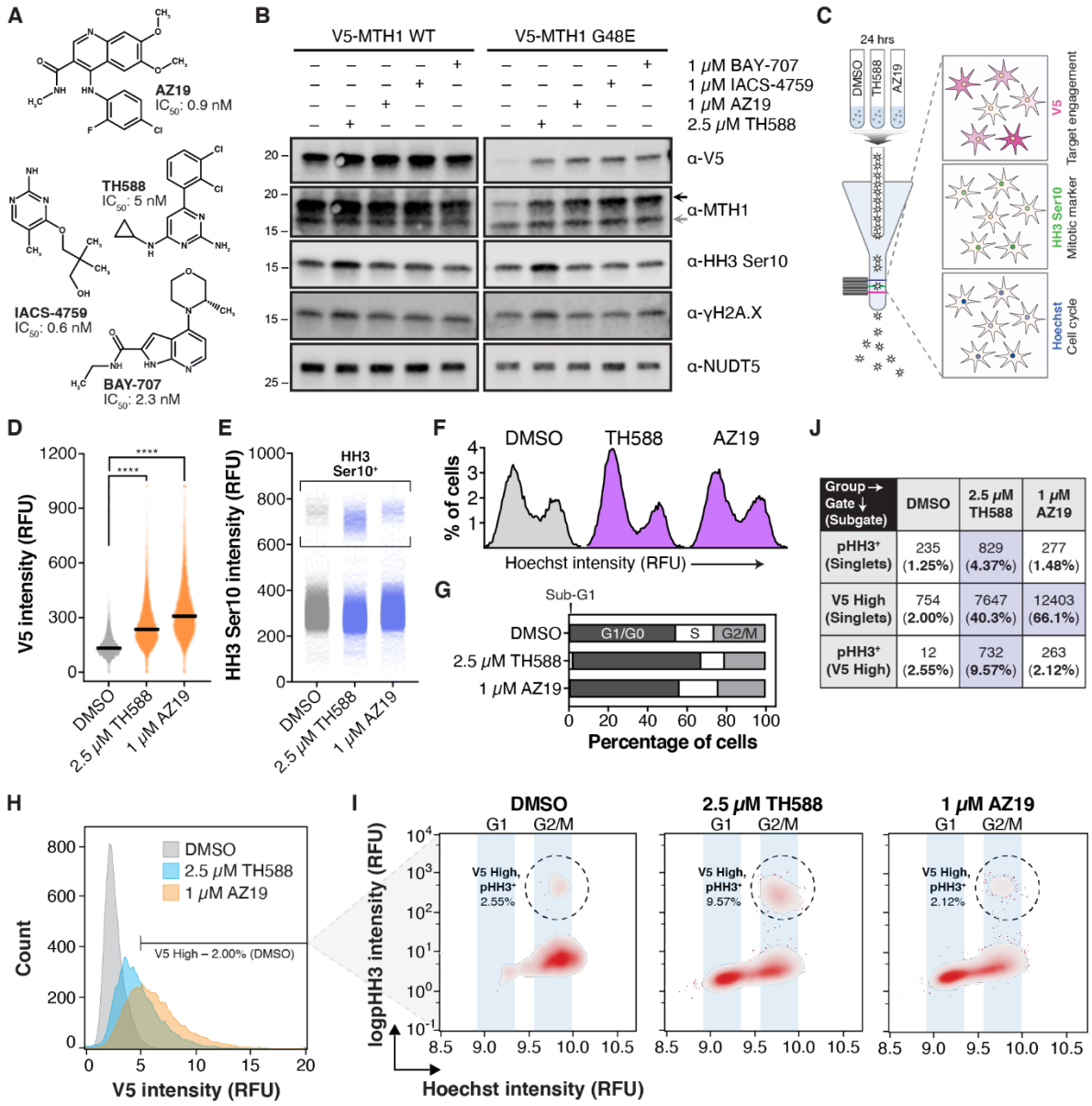

Group → Gate ↓ (Subgate)	DMSO	2.5 μM TH588	1 μM AZ19
pHH3+ (Singlets)	235 (1.25%)	829 (4.37%)	277 (1.48%)
V5 High (Singlets)	754 (2.00%)	7647 (40.3%)	12403 (66.1%)
pHH3+ (V5 High)	12 (2.55%)	732 (9.57%)	263 (2.12%)

Fig. 2. Utilizing V5-MTH1 G48E to uncouple divergent cellular activities from target engagement of structurally dissimilar MTH1 inhibitors. a, MTH1 inhibitors tested and their reported biochemical IC_{50} values[20, 22-24]. **b**, U-2 OS V5-MTH1 WT or V5-MTH1 G48E cells were incubated with DMSO, 2.5 μM TH588, 1 μM AZ19, 1 μM IACS-4759, or 1 μM BAY-707 for 24 hours. Black arrow – V5 MTH1; grey arrow – endogenous, WT MTH1. **c**, A schematic depicting CeTEAM analysis of MTH1 inhibitors with U-2 OS V5-MTH1 G48E clone 6 cells by flow cytometry. **d**, V5, HH3 Ser10 (**e**), and Hoechst intensity (**f**) of cells incubated with DMSO, 2.5 μM TH588, or 1 μM AZ19. n = 20,000 events per sample; line = median. **g**, Proportion of cells by approximated cell cycle phase, sourced from **f**. **h**, Histograms of V5 intensity depicting "V5 high"

events – classified as the top 2% of V5 signal intensity from the DMSO control. **i**, “V5 high” cells were gated and plotted by HH3 Ser10 (y-axis) and Hoechst intensity (x-axis). “V5 high” and pHH3+ cells are identified by dashed circles and the percentages of pHH3+ cells within the “V5 high” population are shown. **j**, Number of positive events and proportion of parental population (in parentheses, %) in specific sub-populations. Significantly changed parameters are highlighted in blue. ns – not significant; **** – $p < 0.0001$ by Kruskal-Wallis test with multiple comparisons to DMSO (Dunn’s test). RFU – relative fluorescence units.

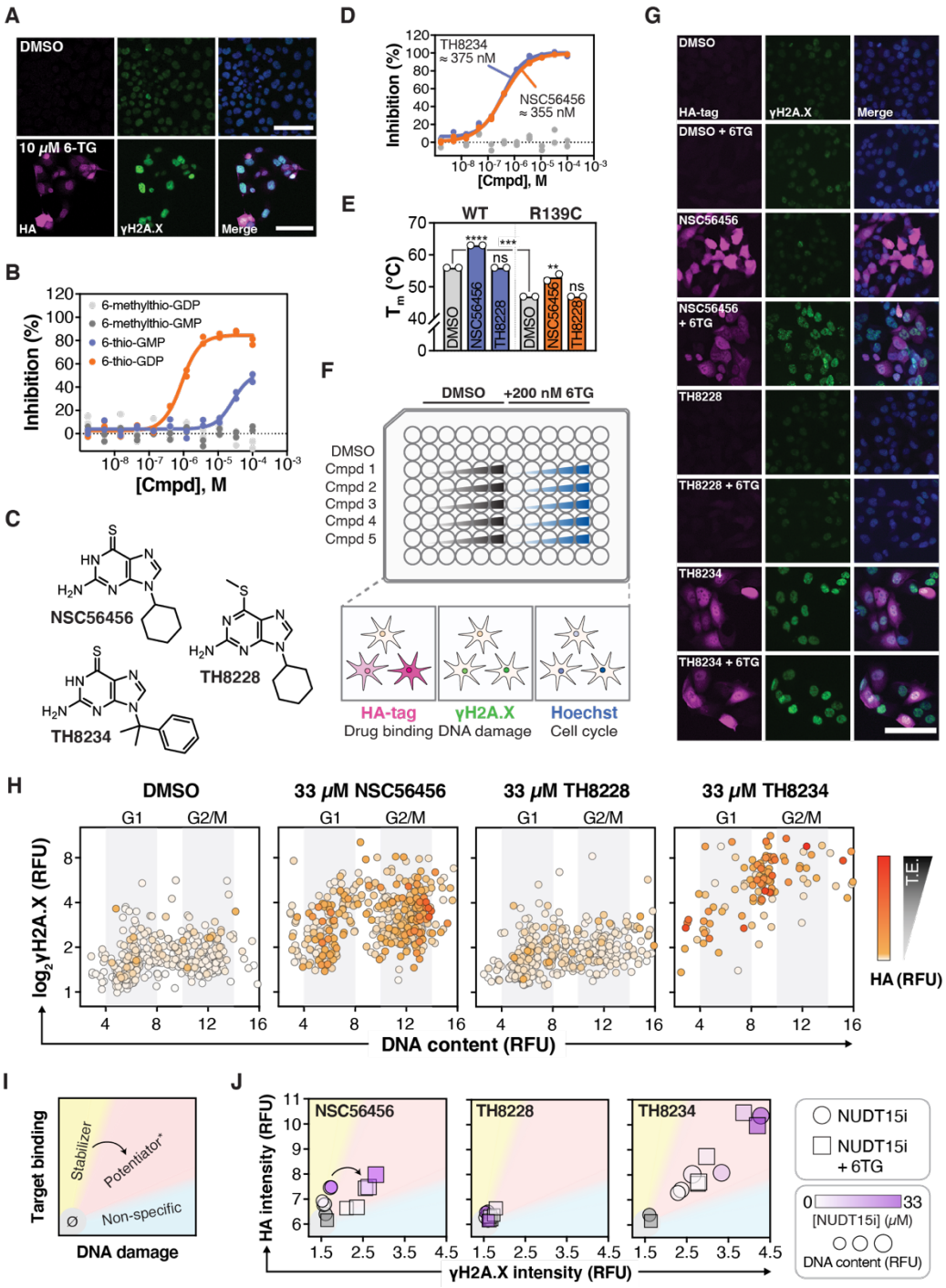

Fig. 3. Repurposing a common missense variant of NUDT15, R139C, to reveal its dynamic interaction with thiopurines and characterize thiopurine-derived NUDT15 inhibitors. a, Fluorescent microscopy images of HCT116 3-6 3xHA-NUDT15 R139C cells, treated with DMSO or 10 μM 6TG for 72 hours, and stained with indicated markers. Hoechst staining is shown in the

merged image. Scale bar = 200 μm. **b**, A representative enzyme-coupled malachite green assay profiling NUDT15 inhibitory capabilities of thiopurine metabolites with dGTP as test substrate (performed in duplicate; line = mean). **c**, The chemical structures of NSC56456, TH8234, and TH8228. **d**, A representative enzyme-coupled malachite green assay testing NUDT15 inhibition by TH8228 (grey), NSC56456 (orange), and TH8234 (blue) thiopurine analogs with dGTP as substrate (performed in duplicate; line = mean). **e**, Compound-induced thermal shifts of NUDT15 WT (blue) and R139C (orange) at 50 μM by DSF assay compared to DMSO (grey). Mean values are shown of n = 2 independent experiments. One-way ANOVA analysis was performed with comparisons to DMSO treatments for each variant (Dunnett's test) and an unpaired t test was used to compare DMSO treatments between WT and R139C. ns – not significant; ** – $p < 0.01$; *** – $p < 0.001$; **** – $p < 0.0001$. **f**, A schematic depicting a high-content microscopy assay for simultaneous detection of target engagement (HA) and phenotypes (γH2A.X and Hoechst) of potential NUDT15 inhibitors -/+ low-dose 6TG. **g**, Representative micrographs of cells pre-treated with DMSO, 33 μM NSC56456, 33 μM TH8228, or 33 μM TH8234, -/+ 6TG, and stained with indicated markers. Hoechst staining is shown in the merged image. Scale bar = 100 μm. **h**, Per-cell three-dimensional analysis of $\log_2$γH2A.X (y-axis), Hoechst (x-axis), and HA intensities (orange-to-red gradient) following treatment with DMSO, 33 μM NSC56456, 33 μM TH8228, or 33 μM TH8234 + 200 nM 6TG. n = at least 100 cells per condition. **i**, Binning of NUDT15i into "non-responder/∅" (grey), "stabilizer" (yellow), "potentiator" (red; expected phenotype), and "non-specific" (blue; unexpected phenotype) based on HA intensity and thiopurine-induced DNA damage. "Stabilizers" may reclassify to "potentiators" in the presence of 6TG. **j**, Per-drug analysis of median HA (y-axis), γH2A.X (x-axis), and Hoechst intensities (symbol size) for NSC56456, TH8228, and TH8234 at multiple concentrations (magenta gradient) and compared to DMSO (grey). NUDT15i alone (circles) or in combination with 6TG (squares). RFU – relative fluorescence units.

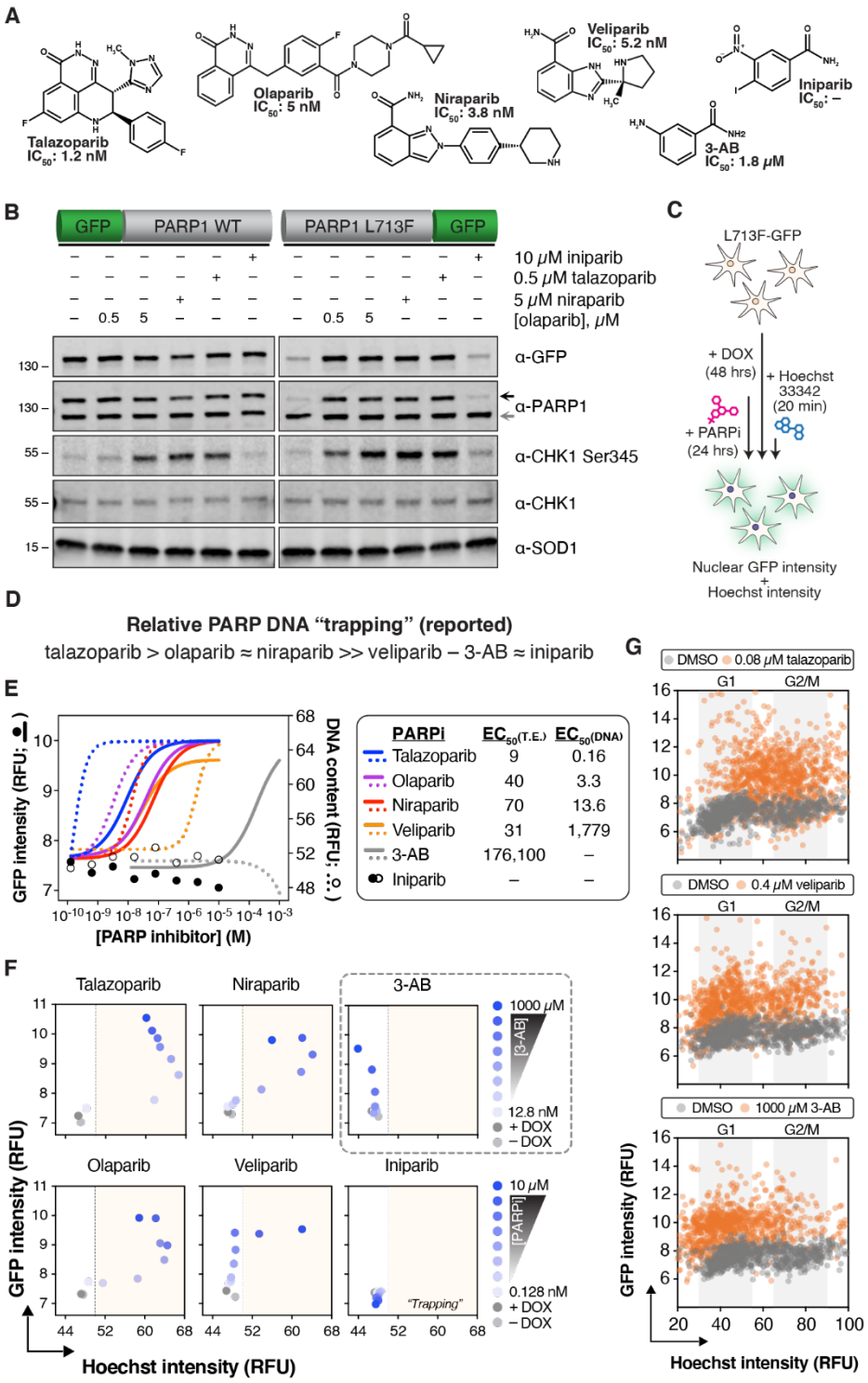

Fig. 4. Profiling of PARPi engagement and trapping in live cells with PARP1 L713F-GFP. a, Chemical structures and PARP1 inhibitory potencies of PARPi studied (SelleckChem and [76]). **b**, GFP-PARP1 WT and L713F-GFP-expressing U-2 OS cells were treated with PARPi for 24 hours.

Black arrow – GFP-tagged PARP1; grey arrow – endogenous PARP1. **c**, Experimental schematic for live cell tracking of PARP1 target engagement (GFP) and PARPi-induced replication stress (Hoechst) by high-content microscopy. **d**, Relative, reported PARP1 trapping potencies of PARPi[36, 41]. **e**, Curve fitting of median GFP (solid) and Hoechst (DNA content; open/dashed) intensities in live U-2 OS PARP1 L713F-GFP clone 5 cells incubated with PARPi for 24 hours. Observed EC_{50} values are shown in nM. Data represent two independent experiments. **f**, Concentration-dependent dynamics of PARP1 target engagement and DNA trapping in live cells after PARPi. Median GFP (y-axis) and Hoechst (x-axis) intensities are shown. Red areas – PARP trapping phenotype. **g**, Simultaneous detection of PARP1 target engagement and cell cycle perturbations in live, individual cells comparing DMSO (grey) and PARPi treatment (orange). Approximate G1 and G2/M cell cycle phases demarcated by grey columns. Overview data representative of n = 500 cells per group per experiment; individual cell plots are n = 1000 cells per group. RFU – relative fluorescence units.

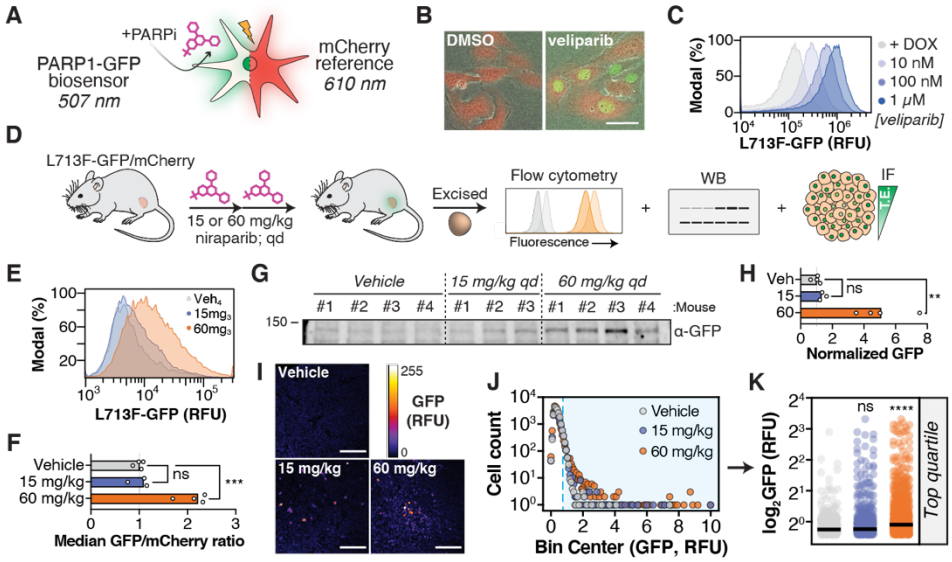

Fig. 5. *In vivo*-optimized CeTEAM PARPi-GFP biosensors for *ex vivo* detection of drug-target engagement. a, The PARP1 L713F-GFP biosensor was paired with mCherry for normalization. **b**, Representative fluorescent micrographs of U-2 OS PARP1 L713F-GFP/mCherry cells treated with DMSO or 1 μM veliparib for 24 hours. Scale bar = 50 μm. **c**, mCherry-normalized L713F-GFP signal from 24-hour veliparib by flow cytometry. Modal normalization is shown. **d**, Graphical overview of *in vivo* experiments with HCT116 PARP1 L713F-GFP/mCherry subcutaneous xenografts treated with either niraparib or vehicle control (2x, qd). $n_{Vehicle}$: 4, $n_{15mg/kg}$: 3, $n_{60mg/kg}$: 4 mice. **e**, Representative flow cytometry histograms of PARP1 L713F-GFP/mCherry tumors. Modal normalization is shown. Veh_4: vehicle mouse #4 (grey), $15mg_3$: 15 mg/kg mouse #3 (blue), and $60mg_3$: 60 mg/kg mouse #3 (orange). **f**, mCherry-normalized L713F-GFP intensity of tumors by flow cytometry. Bars indicate means. **g**, Gross L713F-GFP signal from individual tumors by western blot. **h**, mCherry-normalized L713F-GFP abundance from western blots in **g** and **Extended Data Fig. 7c**. Bars indicate means. **i**, Representative L713F-GFP micrographs from tumor sections with fire LUT. Scale bars = 100 μm. **j**, Histogram of L713F-GFP intensities across tumors and treatment groups. Blue region represents the top quartile of GFP intensity. n = 16,482 total cells per treatment group. **k**, Distribution of individual cell L713F-GFP intensities within the top quartile. Lines show medians. In all cases, ns – not significant, ** – $p < 0.01$, *** – $p < 0.001$, **** – $p < 0.0001$ by one-way ANOVA (Dunnet's test; **f** and **h**) or Kruskal-Wallis test (Dunn's test; **k**) with multiple comparisons to the vehicle. RFU – relative fluorescence units.

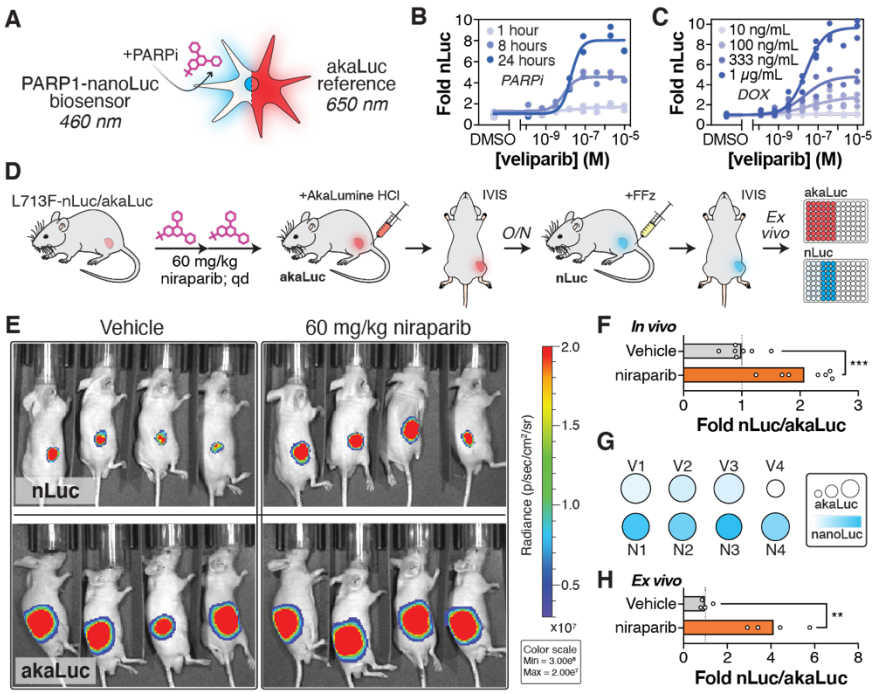

Fig. 6. An *in vivo*-compatible CeTEAM PARPi-nLuc biosensor for multiplexed tracking of drug binding in live animals. a, The PARP1 L713F-nLuc biosensor (em: 460 nm) was paired with akaLuc (em: 650 nm) to enable dual luciferase analyses. **b**, Time-resolved detection of PARP1 L713F-nLuc stabilization in the presence of veliparib treatment and normalized to akaLuc signal. A representative experiment is shown. **c**, Dose-dependent veliparib stabilization over 24 hours for different abundances of PARP1 L713F-nLuc normalized to akaLuc signal. A summary of two independent experiments. **d**, Graphical overview of *in vivo* experiments with PARP1 L713F-nLuc/akaLuc subcutaneous xenografts treated with either vehicle or 60 mg/kg niraparib. n = 7 total mice per group. **e**, Representative bioluminescence overlays of mice treated as in **d** following administration of fluorofurimazine (nLuc) or AkaLumine HCl (akaLuc). **f**, akaLuc-normalized quantification of *in vivo* L713F-nLuc signals from two experimental arms. **g**, *Ex vivo* L713F-nLuc (blue gradient) and akaLuc (circle size) luminescence intensity indicated per tumor. **h**, Quantitation of *ex vivo* L713F-nLuc bioluminescence normalized to akaLuc. For **f** and **h**, ** – $p < 0.01$, *** – $p < 0.001$ by unpaired, two-tailed t test with Welch's correction. In all cases, bars represent mean values.

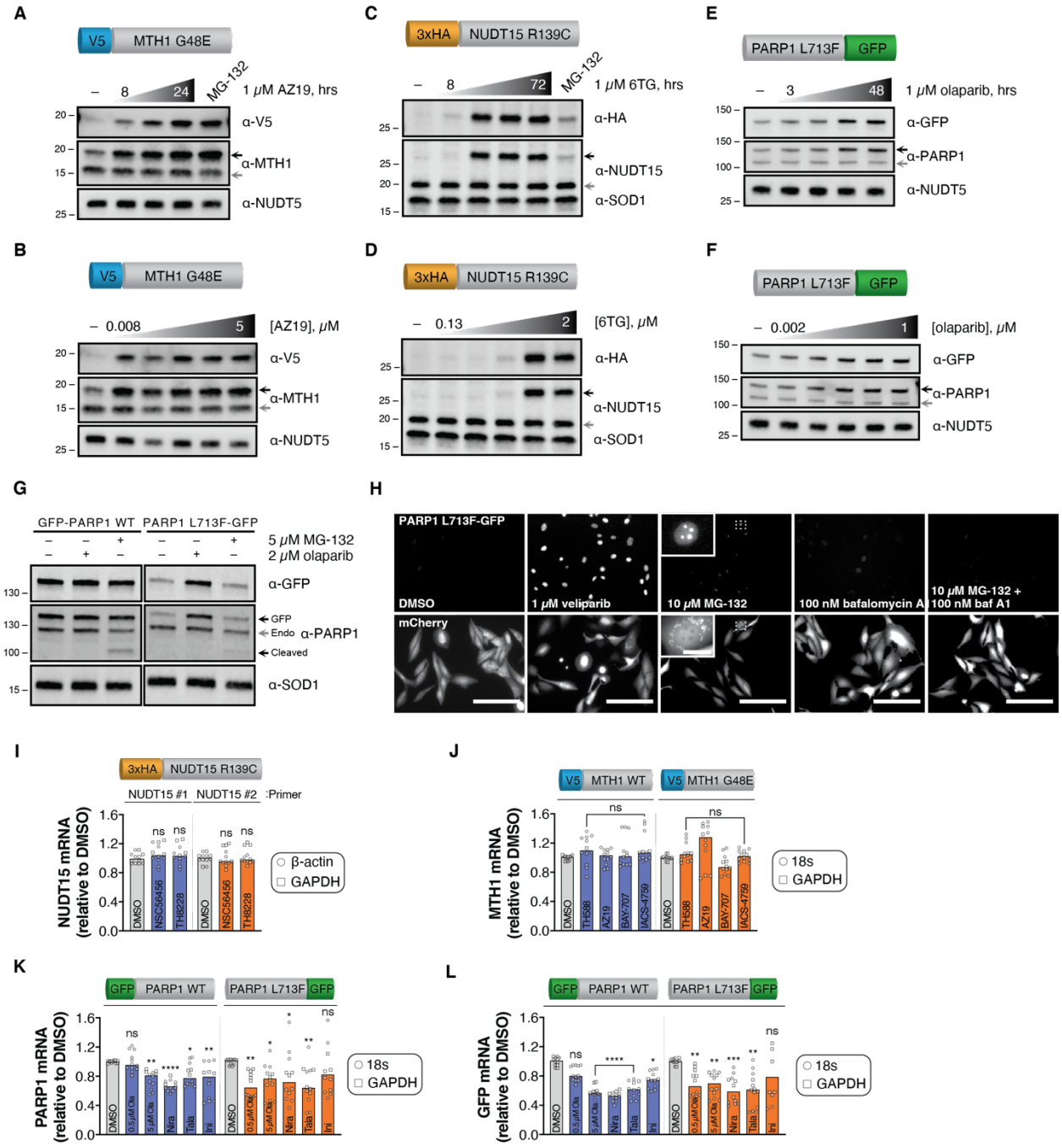

Extended Fig. 1. Characterization of MTH1, NUDT15, and PARP1 drug biosensors. a, U-2 OS V5-MTH1 G48E cells were incubated with DMSO (24 hours), 5 μM MG-132 (6 hours), or 1 μM AZ19 (8-24 hours). **b**, U-2 OS V5-MTH1 G48E cells were incubated with DMSO or AZ19 (0.008-5 μM) for 24 hours. **c**, HCT116 3-6 3xHA-NUDT15 R139C cells were incubated with DMSO (72 hours), 5 μM MG-132 (6 hours), or 1 μM 6TG (8-72 hours). **d**, HCT116 3-6 3xHA-NUDT15 R139C cells were incubated with DMSO or 6TG (0.13-2 μM for 72 hours. **e**, U-2 OS

PARP1 L713F-GFP cells were incubated with DMSO (48 hours) or 1 μM olaparib (3-48 hours). **f**, U-2 OS PARP1 L713F-GFP cells were incubated with DMSO or olaparib (0.0016-1 μM) for 48 hours. **g**, U-2 OS GFP-PARP1 WT or L713F-GFP cells were incubated with DMSO, 2 μM olaparib (24 hours), or 5 μM MG-132 (6 hours) and prepared for western blot with the indicated antibodies. Black arrow – mutant fusion protein; grey arrow – endogenous protein. **h**, U-2 OS PARP1 L713F-GFP/mCherry cells were incubated with DMSO, 1 μM veliparib (24 hours), 10 μM MG-132, 100 nM bafilomycin A1, or 10 μM MG-132 and 100 nM bafilomycin A1 (each for 6 hours) before live cell fluorescence microscopy. Scale bar is 200 μm and 20 μm for inset. **i**, HCT116 3-6 3xHA-NUDT15 R139C cells were treated with DMSO, 20 μM NSC56456, or 20 μM TH8228 for 24 hours before RT-qPCR analysis. **j**, U-2 OS V5-MTH1 WT or G48E cells were treated with DMSO, 2.5 μM TH588, 1 μM AZ19, 1 μM BAY-707, or 1 μM IACS-4759 for 24 hours before RT-qPCR analysis. **k**, U-2 OS GFP-PARP1 WT or PARP1 L713F-GFP cells were treated with DMSO, 0.5 or 5 μM olaparib, 5 μM niraparib, 0.5 μM talazoparib, or 10 μM iniparib for 24 hours before RT-qPCR analysis. Total PARP1 transcripts or GFP transcripts (**l**) were quantified. In all cases, ns – not significant; * – $p < 0.05$; ** – $p < 0.01$; *** – $p < 0.001$; **** – $p < 0.0001$ by Kruskal-Wallis test with multiple comparisons to DMSO controls for each primer or cell set (Dunn's test). Each RT-qPCR set summarizes two independent experiments run in triplicate and normalized to each housekeeping gene. Bars indicate median values.

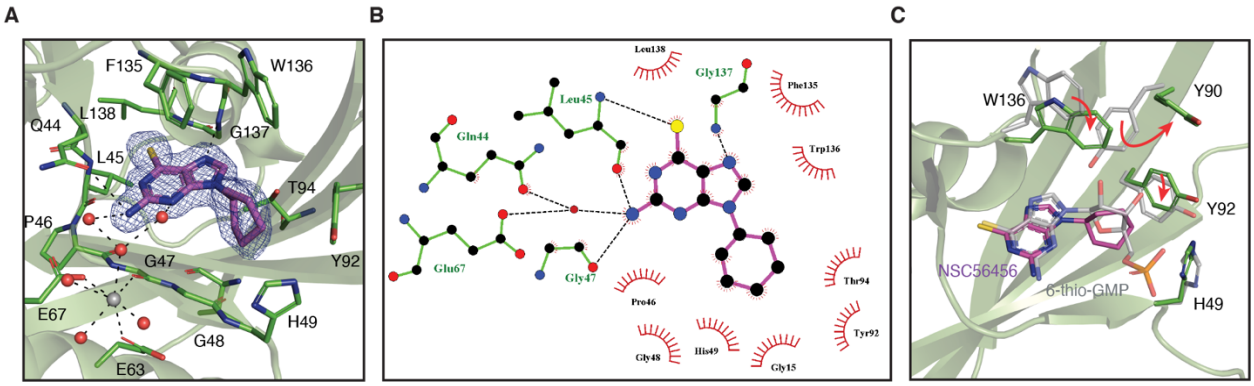

Extended Fig. 2. NUDT15-NSC56456 co-crystal structure. **a**, Co-crystal structure of NSC56456 bound to the catalytic site of WT NUDT15 with binding interactions. NSC56456 is depicted in magenta (with $2F_o$-F_c electron density map in blue), interacting NUDT15 residues are in bright green, magnesium ions in grey, and water molecules in red. Hydrogen bonding interactions are depicted by dashed, black lines. **b**, Ligplot+ representation of NSC56456 binding interactions in the NUDT15 active site. Residues interacting with NSC56456 (magenta) are shown in green. Hydrophobic interactions are shown as an arc with spokes and hydrogen bonds as dashed lines. **c**, Binding modality comparison of NSC56456 and 6-thio-GMP within NUDT15. The aligned 6-thio-GMP-bound structure of NUDT15 (PDB ID: 5LPG) is shown in grey, while the NUDT15-NSC56456 structure is green. Residues that undergo a significant conformational change between the two structures are highlighted. The 6-thioguanine group is positioned in nearly the exact same position in both structures, aside from a slight tilt. This tilt strengthens several hydrogen bonds by bringing the bonding partners into closer proximity (bonding to Leu45 is decreased by 0.1 Å and Gly137 by 0.4 Å, respectively, **b**). The cyclohexane ring is situated similarly to ribose in the 6-thio-GMP structure, but since it lacks the protruding hydroxyl groups, this leaves empty space in the binding pocket. Trp136 has moved into the active site by 2.9 Å to fill this empty space, which causes Tyr90 to be flipped outwards.

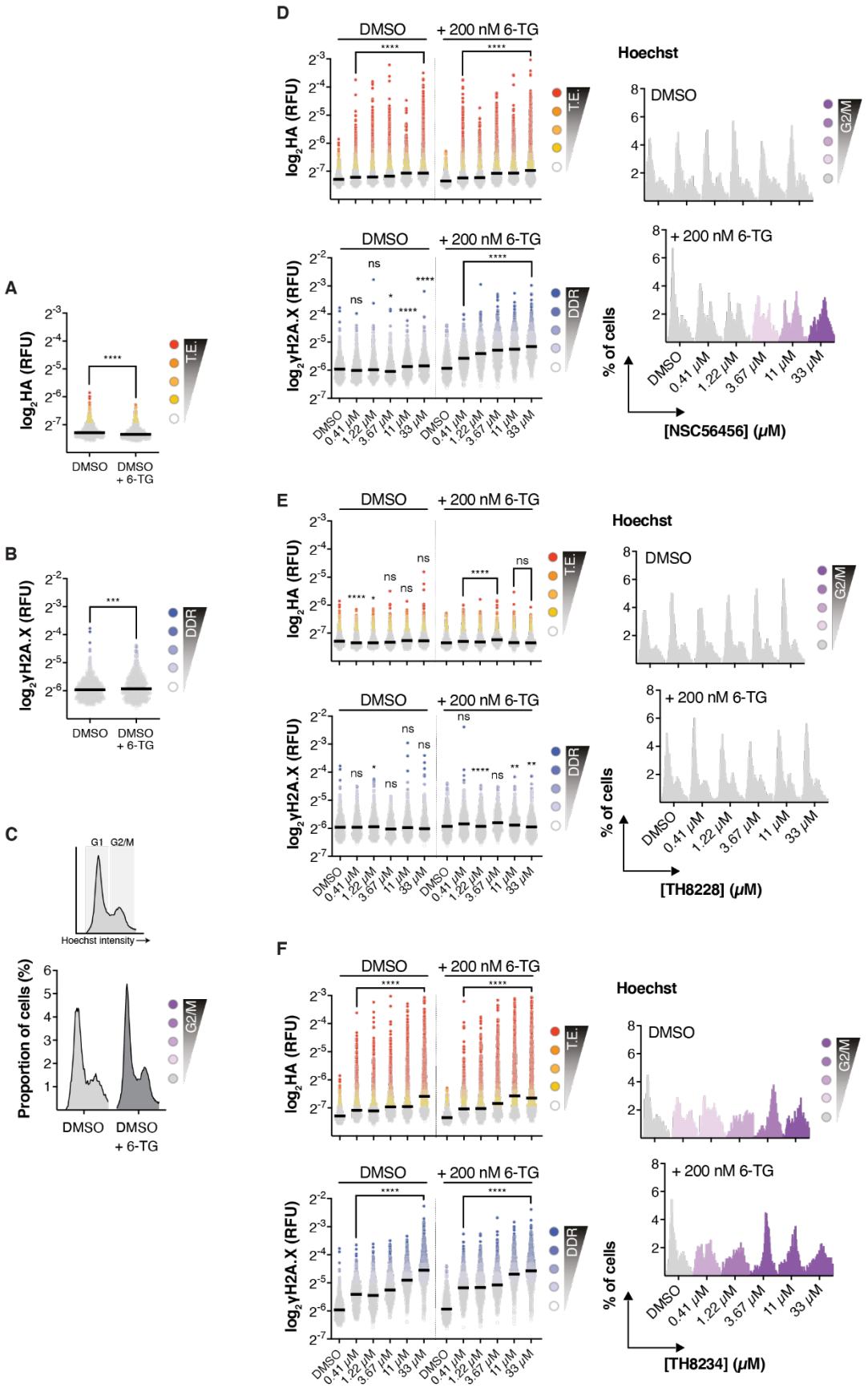
A
log2HA (RFU)
T.E.
DMSO
DMSO + 6-TG
B
log2γH2A.X (RFU)
DDR
C
G1
G2/M
Hoechst intensity
Proportion of cells (%)
D
DMSO
+ 200 nM 6-TG
Hoechst
% of cells
[NSC56456] (μM)
E
[TH8228] (μM)
F
[TH8234] (μM)

Extended Fig. 3. Assessment of thiopurine-derived NUDT15 inhibitors with pooled HCT116 3-6 3xHA-NUDT15 R139C cells. a, Log_2HA, (**b**) log_2γH2A.X, and (**c**) Hoechst intensities of individual HCT116 3-6 3xHA-NUDT15 R139C cells treated with DMSO or 200 nM 6TG for 72 hours (n = 1000 cells per condition). Increasing concentrations of NSC56456 (**d**), TH8228 (**e**), or TH8234 (**f**) were incubated, as in **Fig. 3f,** and measured for HA, γH2A.X, and Hoechst intensity. Data related to **Fig. 3g-j**. n = 1000 cells per condition. In all cases, ns – not significant; * – $p < 0.05$; ** – $p < 0.01$; *** – $p < 0.001$; **** – $p < 0.0001$ by Kruskal-Wallis test with comparison to the DMSO control for each set (Dunn's test; **d-f**) or t-test (**a-c**). Representative experiments are shown, and lines indicate median values. RFU – relative fluorescence units. Yellow-to-red gradient – increasing target engagement (T.E.); blue gradient – increasing DNA damage response (DDR); purple gradient – increasing G2/M cell cycle content (G2/M).

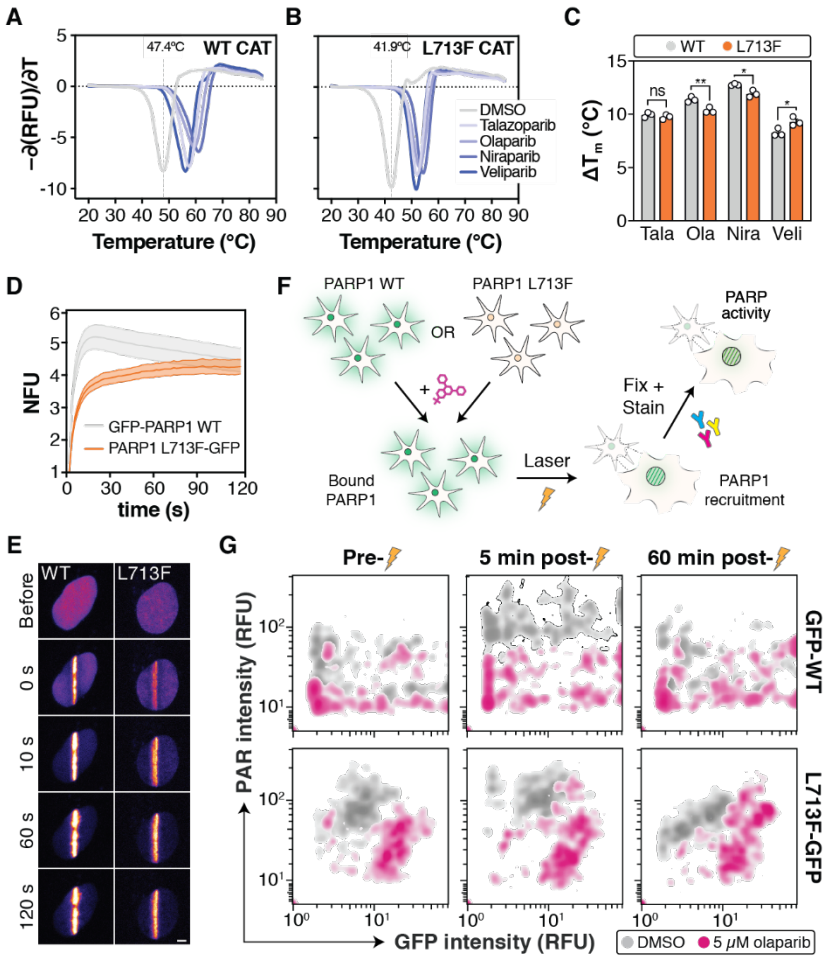

Extended Fig. 4. PARP1 L713F is a *bona fide* PARPi biosensor. a, Representative DSF with 5 μM PARP1 WT or (**b**) L713F catalytic domain with DMSO or 250 μM PARPi displayed as the negative first derivative. Melting temperatures (T_m) of DMSO controls are shown. **c**, The change in melting temperature relative to DMSO (ΔT_m) calculated from **a** and **b**. ns – not significant; * – $p < 0.05$; ** – $p < 0.01$ by multiple unpaired t test with Welch's correction. n = 3 independent experiments with means shown. **d**, Quantification of live-cell recruitment kinetics for GFP-PARP1 WT and PARP1 L713F-GFP to laser microirradiation-induced DNA damage sites. Mean values ± SEM are shown from five independent experiments. NFU – normalized fluorescence units. **e**, Representative snapshots of PARP1 saturation at microirradiation-induced DNA breaks. Scale bar = 5 μm. **f**, Graphical procedure for monitoring PARP-GFP intensity and activity at DNA damage sites in the presence of PARPi. **g**, Dynamics of WT or L713F PARP1-GFP stabilization and PAR abundance in the absence (grey) or presence (magenta) of olaparib for 1 hour (corresponding data

in **Extended Fig. 5a-d**) by density plot. n = 229 cells per group from three independent experiments. NFU – normalized fluorescence units, RFU – relative fluorescence units.

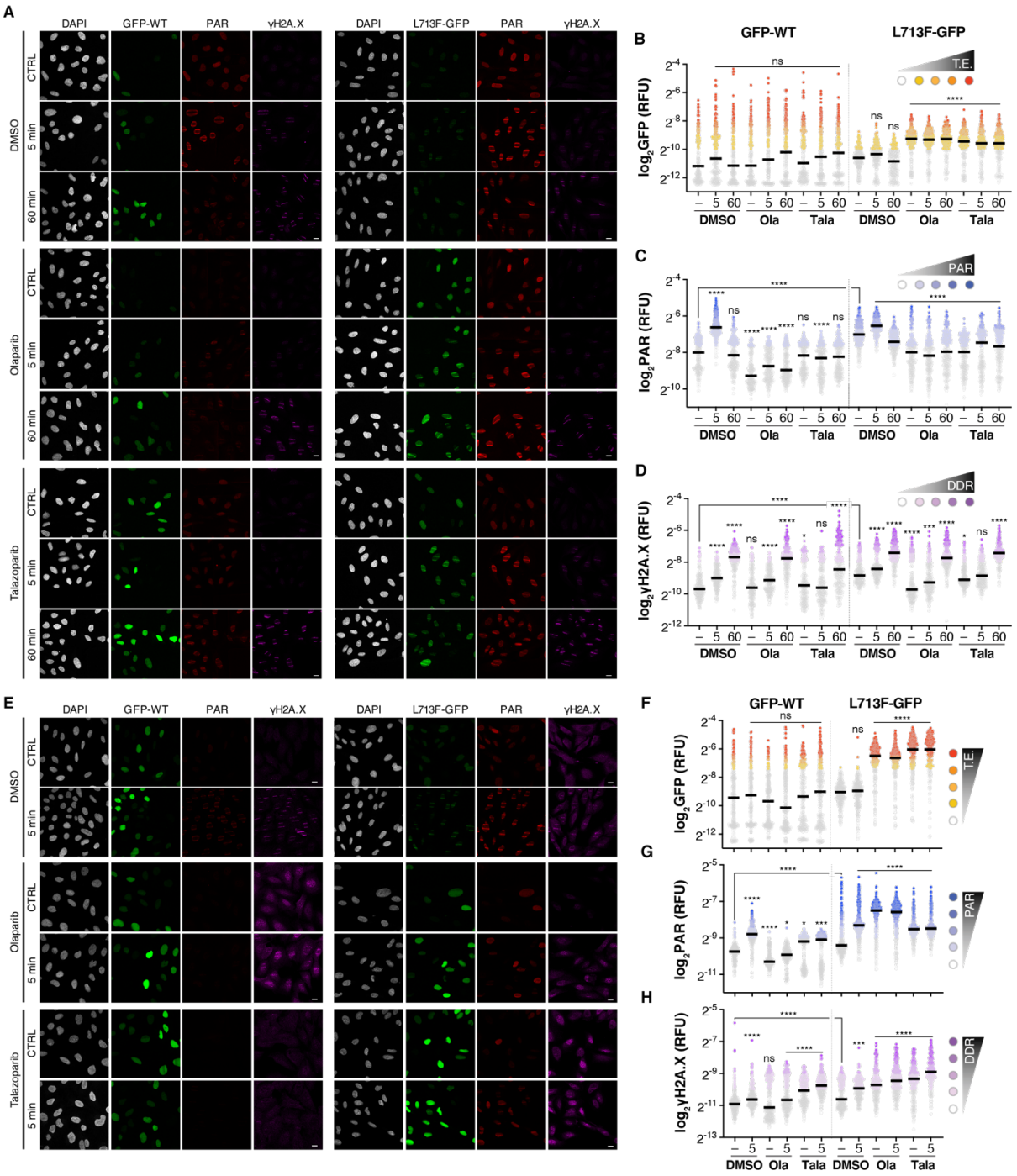

Extended Fig. 5. Dynamics of GFP-PARP1 WT and PARP1 L713F-GFP recruitment to sites of DNA damage in the absence or presence of clinical PARPi. a, U-2 OS GFP-PARP1 WT or PARP1 L713F-GFP cells were pre-treated with DMSO, 5 μM olaparib, or 0.5 μM talazoparib for 1 hour before microirradiation and fixation after 5 or 60 minutes. **b**, Plots of $\log_2$GFP intensity, **c**, $\log_2$PAR intensity, and **d**, $\log_2$γH2A.X intensity for individual cells following 1-hour pre-treatment

with PARPi. **e**, Cells were pre-treated with DMSO, 5 μM olaparib, or 0.5 μM talazoparib for 24 hours prior to microirradiation and fixation after 5 minutes. For all micrographs, DAPI – blue; GFP-PARP1 – green; PAR – red; γH2A.X – magenta and scale bar = 20 μm. **f**, Plots of $\log_2$GFP intensity, **g**, $\log_2$PAR intensity, and **h**, $\log_2$γH2A.X intensity for individual cells following 24-hour pre-treatment with PARPi. For microscopy datasets, n= 229 cells from three independent experiments. Bars represent median values. Kruskal-Wallis analyses were performed with comparisons to DMSO treatments for each group (Dunn's test) and a Mann-Whitney test was used to compare DMSO treatments between WT and L713F (**b-d** and **f-h**). ns – not significant; * – $p < 0.05$; *** – $p < 0.001$, **** – $p < 0.0001$. RFU – relative fluorescence units; NFU – normalized fluorescence units; yellow-to-red gradient – increasing target engagement (T.E.); blue gradient – increasing polyADP-ribose (PAR); purple gradient – increasing DNA damage response (DDR) *via* γH2A.X.

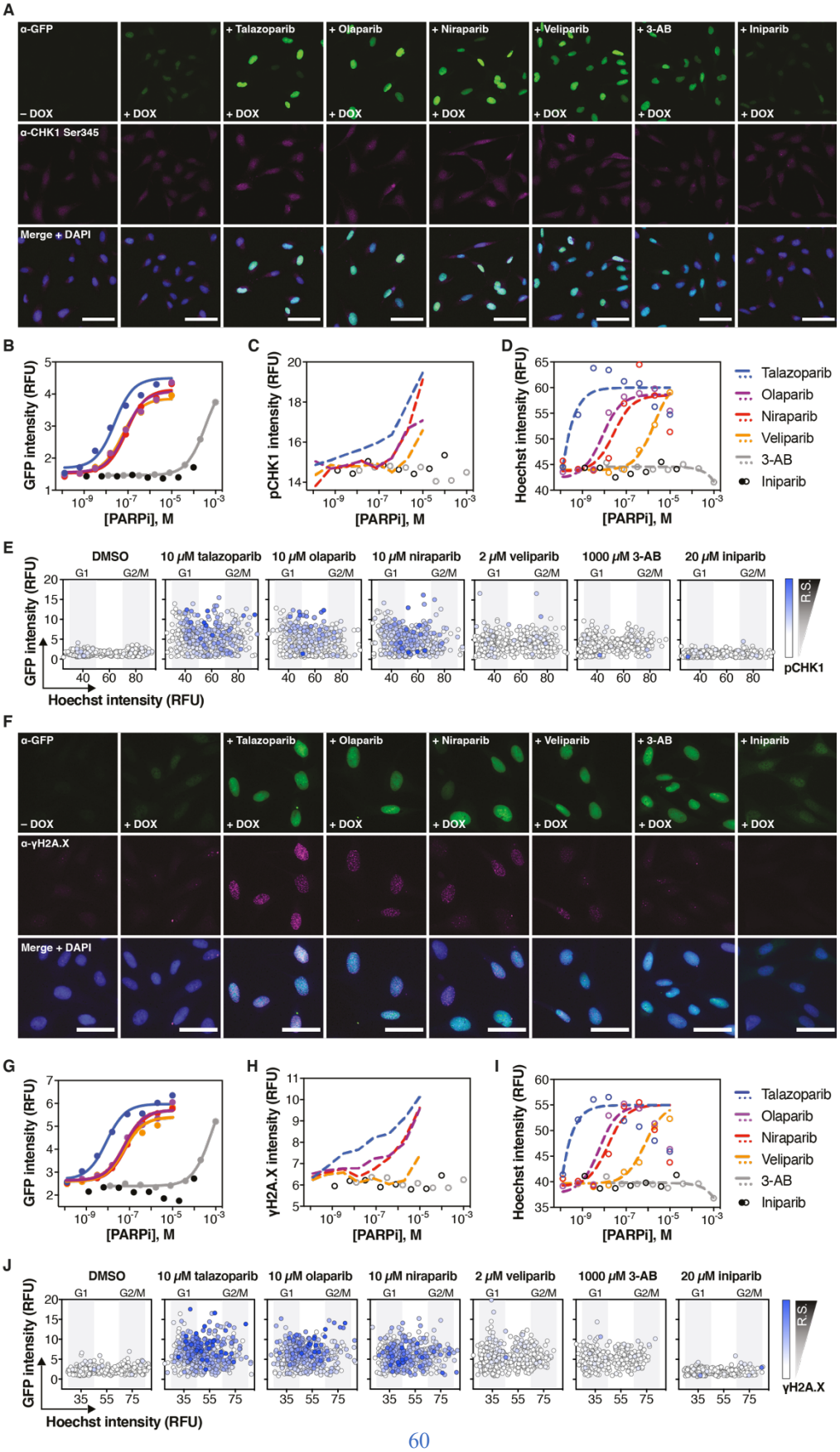
A
α-GFP
– DOX
+ DOX
+ Talazoparib
+ Olaparib
+ Niraparib
+ Veliparib
+ 3-AB
+ Iniparib
α-CHK1 Ser345
Merge + DAPI
B
GFP intensity (RFU)
[PARPi], M
C
pCHK1 intensity (RFU)
D
Hoechst intensity (RFU)
Talazoparib
Olaparib
Niraparib
Veliparib
3-AB
Iniparib
E
DMSO
10 μM talazoparib
10 μM olaparib
10 μM niraparib
2 μM veliparib
1000 μM 3-AB
20 μM iniparib
G1
G2/M
R.S.
pCHK1
F
α-γH2A.X
G
H
γH2A.X intensity (RFU)
I
J
γH2A.X

Extended Fig. 6. Multiparametric interrogation of fixed PARP1 L713F-GFP-expressing cells exposed to PARP inhibitors. a, Representative micrographs of U-2 OS PARP1 L713F-GFP clone #5 cells incubated with increasing concentrations of talazoparib, olaparib, niraparib, veliparib, iniparib, or 3-AB for 24 hours and stained for GFP (target engagement), CHK1 Ser345 (pCHK1; replication stress/DNA damage), and Hoechst 33342 (DNA content; in merged image). Scale bar = 200 μm. Median GFP (**b**), CHK1 Ser345 (**c**), and Hoechst (**d**) intensities. **e**, Per-cell, three-dimensional visualization of GFP (y-axis), Hoechst (x-axis), and CHK1 Ser345 (blue gradient) after DMSO, 10 μM talazoparib, 10 μM olaparib, 10 μM niraparib, 2 μM veliparib, 1000 μM 3-AB or 20 μM iniparib. Estimated G1 and G2/M cell populations are demarcated. n = 500 cells shown per condition. **f**, Representative micrographs of U-2 OS PARP1 L713F-GFP clone #5 cells incubated with increasing concentrations of talazoparib, olaparib, niraparib, veliparib, iniparib, or 3-AB for 24 hours and stained for GFP, γH2A.X (replication stress/DNA damage), and Hoechst 33342 (in merged image). Scale bar = 50 μm. Median GFP (**g**), γH2A.X (**h**), and Hoechst (**i**) intensities. **j**, Per-cell three-dimensional visualization of GFP (y-axis), Hoechst (x-axis), and γH2A.X (blue gradient) after DMSO, 10 μM talazoparib, 10 μM olaparib, 10 μM niraparib, 2 μM veliparib, 1000 μM 3-AB or 20 μM iniparib. Estimated G1 and G2/M cell populations are demarcated. 500 cells per condition are shown. In all cases, representative experiments and lines of best fit are shown; RFU – relative fluorescence units and blue gradient – increasing replication stress/DNA damage (CHK1 Ser345 or γH2A.X; R.S.).

A

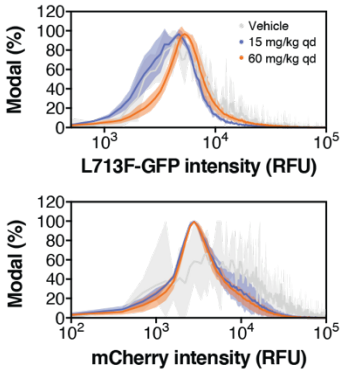

B

Mouse	Median GFP (RFU)	Median mCherry (RFU)
V1	9864	25849
V2	14435	30346
V3	17162	37577.5
V4	5071	11648
15-1	5157	10679
15-2	5173	15520
15-3	6343	12541
60-1	9762	10438
60-2	11968	11781
60-3	12521	16875.5
60-4	10255.5	9937

C

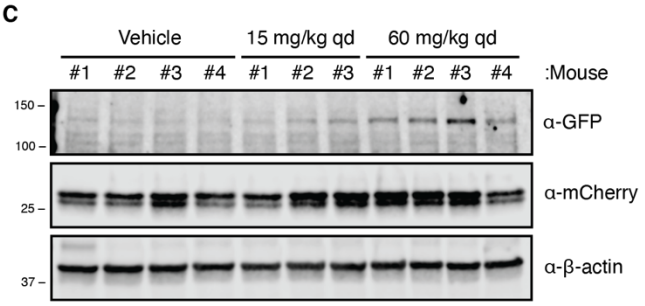

D

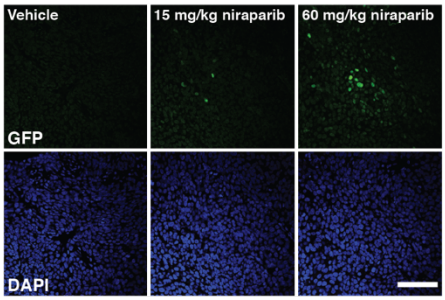

E

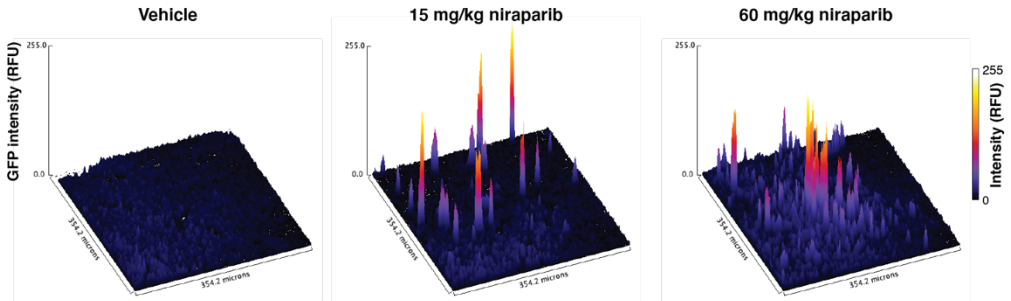

F

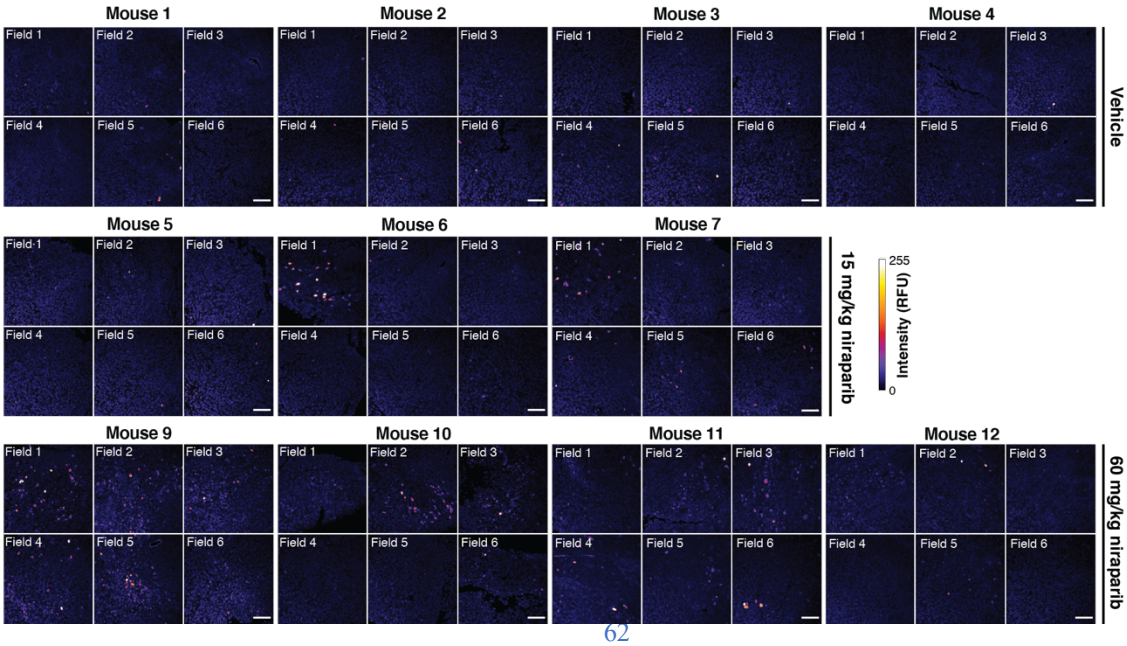

1

Extended Fig. 7. *Ex vivo* analyses of PARP1 L713F-GFP target engagement in mice. a, Average L713F-GFP and mCherry intensity histograms from flow cytometry of live HCT116 tumor cells. Histograms are normalized to the mode for each dataset. The error bands denote the data ranges from $n_{Vehicle} = 4$, $n_{15mg/kg} = 3$, and $n_{60mg/kg} = 4$ mice. **b**, Median L713F-GFP and mCherry fluorescence intensities from tumor cells used to calculate fold change of PARPi target engagement. **c**, Full western blot from **Fig. 5g**, including mCherry and β-actin loading controls. **d**, anti-GFP staining of representative PARP1 L713F-GFP/mCherry tumor sections counterstained with DAPI. Scale bar = 100 µm. **e**, Surface plots of representative tumor sections showing GFP saturation by fire LUT (0 to 255 pixel intensity scaling). **f**, Micrographs of L713F-GFP saturation in tumor sections by fire LUT. Six fields were taken per section. RFU – relative fluorescence units.

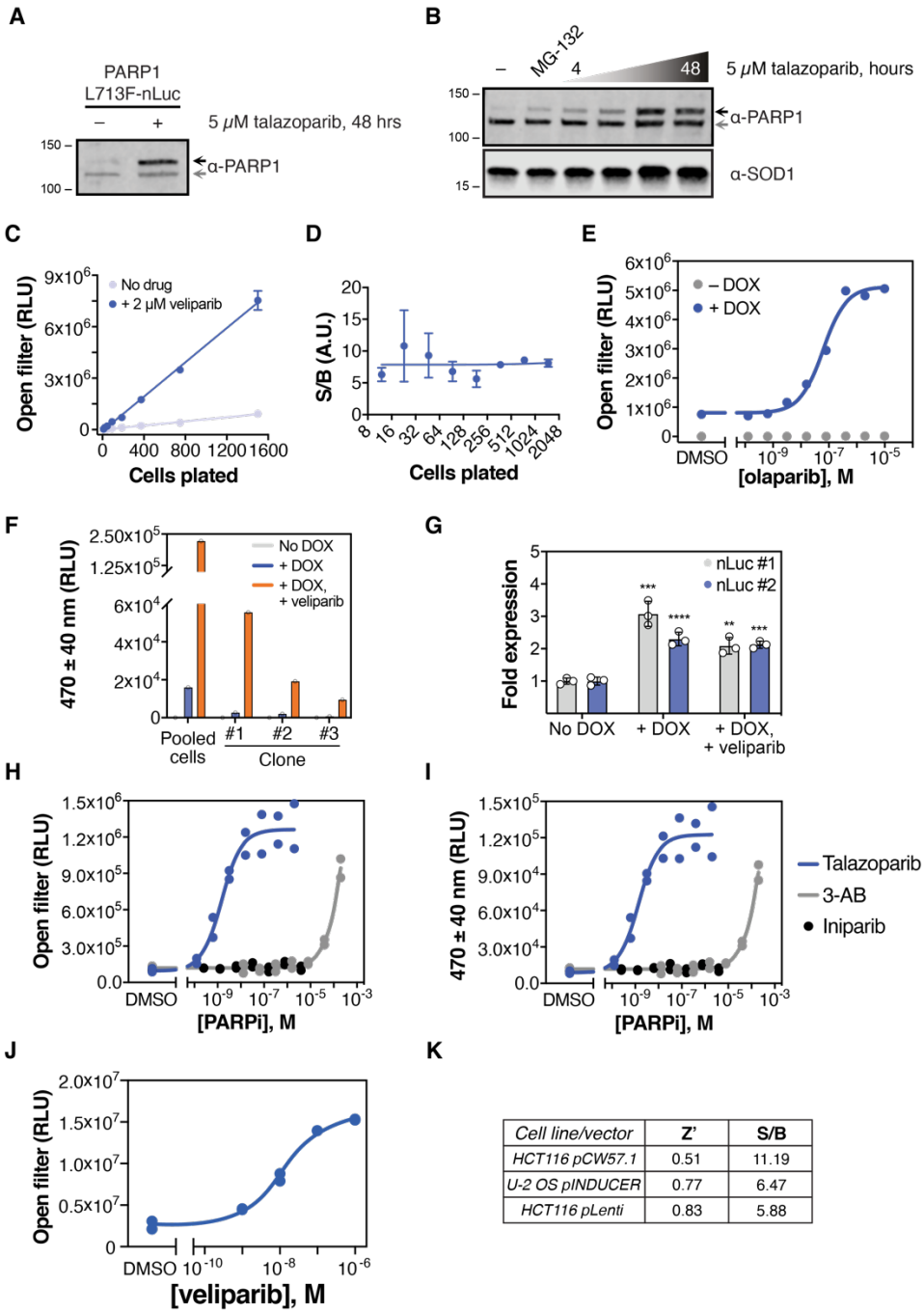

Cell line/vector	Z'	S/B
HCT116 pCW57.1	0.51	11.19
U-2 OS pINDUCER	0.77	6.47
HCT116 pLenti	0.83	5.88

Extended Fig. 8. Assessment of PARP1 L713F-nLuc stabilization by PARPi. a, U-2 OS PARP1 L713F-nLuc #3 cells pre-treated with 1 μg/mL DOX were exposed to DMSO or 5 μM talazoparib for 48 hours. **b**, Cells (as in **a**) were treated with 5 μM talazoparib for 4-48 hours. As controls, DMSO was added for 48 hours and 5 μM MG-132 for 6 hours. Black arrow – PARP1 L713F-nLuc; grey arrow – endogenous PARP1. **c**, Cells (as in **a**) were plated at different densities and treated with DMSO or 2 μM veliparib for an additional 24 hours the following day before

luminescence readings. Linear regressions are shown for both data sets. **d**, Signal-to-background calculations across different cell numbers plated (from **Extended Fig. 8c**). Linear regression illustrates the consistency of the S/B. **e**, Cells plated in the absence or presence of 1 μg/mL DOX were exposed to DMSO or serial dilutions of olaparib for 24 hours prior to luminescence detection. **f**, Pooled or clonal HCT116 pCW57.1-PARP1 L713F-nLuc cells were plated in the absence or presence of 1 μg/mL DOX and then 1 μM veliparib for 24 hours. **g**, Fold of expression of nLuc in pooled HCT116 pCW57.1-PARP1 L713F-nLuc cells after normalization to GAPDH and β-actin by RT-qPCR. Means ± SD are shown. In all cases, ** – $p < 0.01$; *** – $p < 0.001$; **** – $p < 0.0001$ by one-way ANOVA with multiple comparisons to "No DOX" for each primer pair (Dunnett's test). **h**, After induction, HCT116 pCW57.1-PARP1 L713F-nLuc cells were treated with serial dilutions of talazoparib, 3-AB, or iniparib diluted in Fluorobrite DMEM for an additional 24 hours before luminescence detection on an open filter setting. **i**, The same experiment from **Extended Fig. 8h** but measured on a nLuc-specific filter. **j**, HCT116 pLenti CMV Blast-PARP1 L713F-nLuc cells were treated with DMSO or veliparib for 24 hours before measuring luminescence. **k**, A comparison of Z' and signal-to-background (S/B) values across cell systems. $Z' = 1 - [3\sigma_+ + 3\sigma_-] / |\mu_+ - \mu_-|$ and S/B = [mean signal] / [mean background], as defined by Zhang, Chung, & Oldenburg[48]. RLU – relative luminescence units.

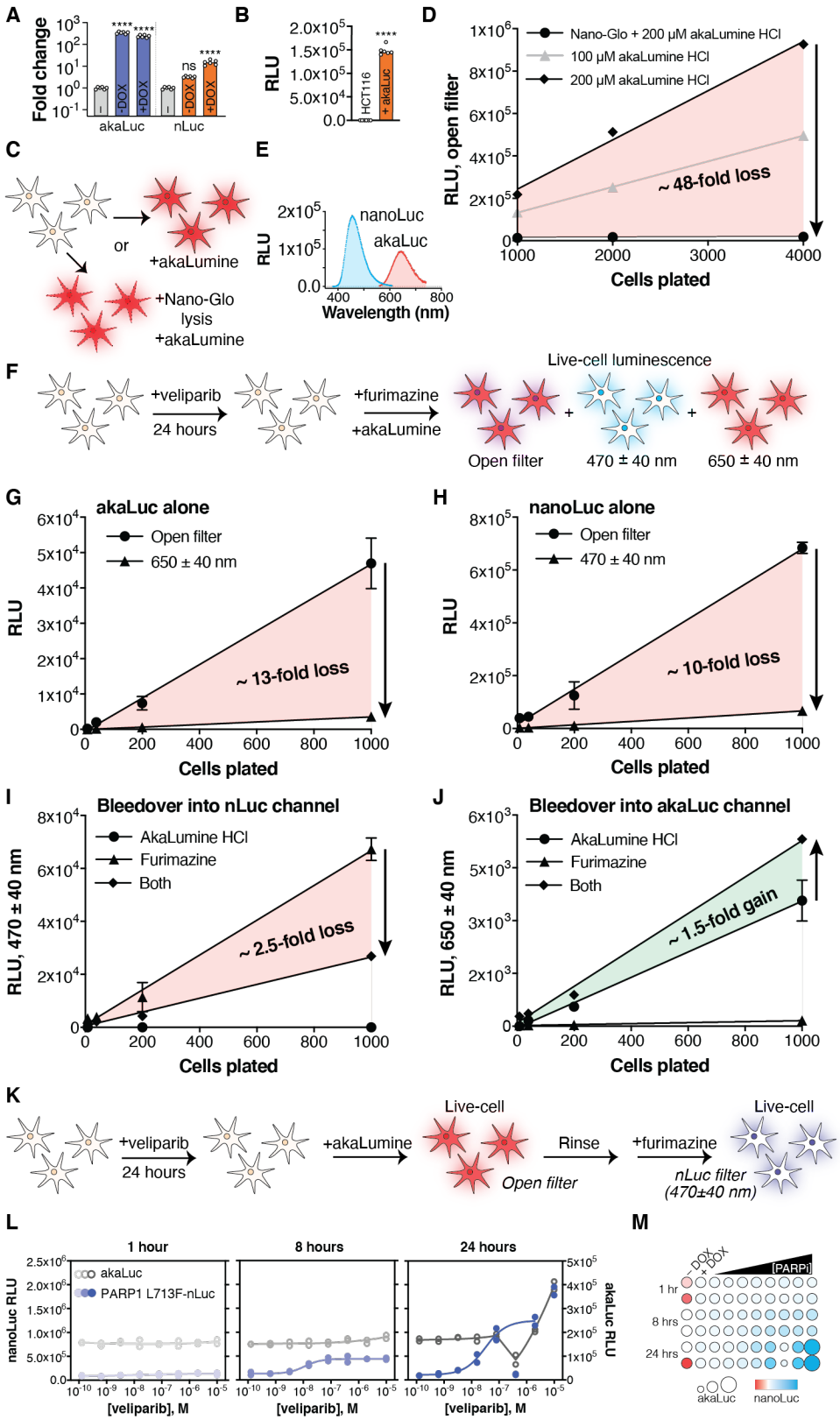
A
Fold change
-DOX
+DOX
akaLuc
nLuc
ns
B
RLU
HCT116
+ akaLuc
C
or
+akaLumine
+Nano-Glo
lysis
+akaLumine
D
Nano-Glo + 200 μM akaLumine HCl
100 μM akaLumine HCl
200 μM akaLumine HCl
RLU, open filter
~ 48-fold loss
Cells plated
E
nanoLuc
akaLuc
RLU
Wavelength (nm)
F
+veliparib
24 hours
+furimazine
+akaLumine
Live-cell luminescence
Open filter
470 ± 40 nm
650 ± 40 nm
G
akaLuc alone
Open filter
650 ± 40 nm
RLU
~ 13-fold loss
Cells plated
H
nanoLuc alone
Open filter
470 ± 40 nm
RLU
~ 10-fold loss
Cells plated
I
Bleedover into nLuc channel
AkaLumine HCl
Furimazine
Both
RLU, 470 ± 40 nm
~ 2.5-fold loss
Cells plated
J
Bleedover into akaLuc channel
AkaLumine HCl
Furimazine
Both
RLU, 650 ± 40 nm
~ 1.5-fold gain
Cells plated
K
+veliparib
24 hours
+akaLumine
Live-cell
Open filter
Rinse
+furimazine
Live-cell
nLuc filter
(470±40 nm)
L
1 hour
8 hours
24 hours
akaLuc
PARP1 L713F-nLuc
nanoLuc RLU
akaLuc RLU
[veliparib], M
M
-DOX
+DOX
[PARP]
1 hr
8 hrs
24 hrs
akaLuc
nanoLuc

Extended Fig. 9. AkaLuc suitability as an nLuc normalization factor. a, RT-qPCR analysis of parental HCT116 (–; grey) or HCT116 pCW57.1-PARP1 L713F-nLuc/pLenti CMV Blast-akaLuc cells treated with -/+ DOX for 24 hours. akaLuc (blue) and nLuc (orange) fold expression was determined by normalization to GAPDH and β-actin and plotted in $\log_{10}$ scale. n = 2 independent experiments in triplicate. **b**, Cells were treated as in **a**, then incubated with 200 μM akaLumine HCl immediately before measurement. n = 2 independent experiments in triplicate. **c**, Graphical procedure for determining akaLuc amenability to lytic conditions. **d**, Induced HCT116 pCW57.1-PARP1 L713F-nLuc/pLenti CMV Blast-akaLuc cells plated at different densities were incubated with 200 μM akaLumine HCl in Nano-Glo lysis reagent or at 100 or 200 μM in FluoroBrite DMEM immediately before luminescence readings. **e**, Emission and intensity spectra of L713F-nLuc and akaLuc. **f**, Graphical procedure of concomitant measuring of nLuc and akaLuc signals following 1 μM veliparib treatment in live HCT116 pCW57.1-PARP1 L713F-nLuc/pLenti CMV Blast-akaLuc cells. **g**, Comparison of akaLuc detection using an open filter or akaLuc-specific filter, as in **f**. **h**, Comparison of L713F-nLuc detection using an open filter or nLuc-specific filter, as in **f**. **i**, Comparison of nLuc filter signal when cells are incubated with akaLumine HCl, furimazine, or both simultaneously at different plating numbers. **j**, Comparison of akaLuc filter signal, as in **i**. **k**, Graphical procedure for sequential measurement of akaLuc followed by L713F-nLuc in live cells. **l**, Time-dependent maturation of L713F-nLuc signal compared to akaLuc signal. **m**, Normalization matrix for L713F-nLuc to akaLuc. Circle size: akaLuc intensity; red-white-blue gradient: nLuc intensity. RLU – relative luminescence units. Bars show median values and lines are best fit. In all cases, ns – not significant; **** – $p < 0.0001$ by one-way ANOVA analysis with multiple comparisons to parental HCT116 cells for each primer set (Dunnett's test; **a**) or Welch's two-tailed t test (**b**).

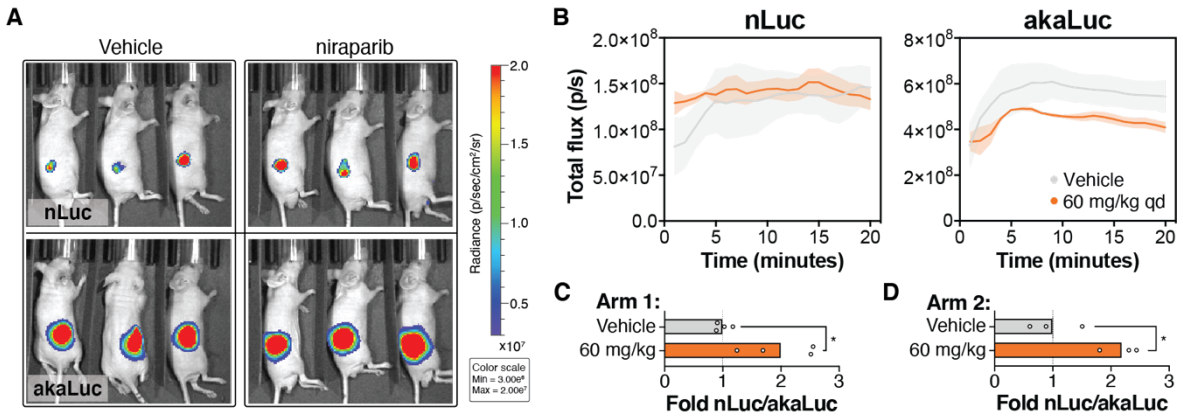

Extended Fig. 10. The second arm of the L713F-nLuc dual luciferase experiment evaluating PARPi binding in live animals. a, Representative bioluminescence overlays for L713F-nLuc and akaLuc radiance. **b**, Change in total luminescent flux (photons/second) over 20 minutes for both L713F-nLuc and akaLuc following substrate injection in mice treated with vehicle or 60 mg/kg niraparib. n = 3 mice per group; error bands denote the SEM. Comparison of the mean fold change in L713F-nLuc/akaLuc signal from experimental arm 1 (**c**, n = 4 mice per group) and arm 2 (**d**, n = 3 mice per group). * – $p < 0.05$ by two-tailed t test.